A SEMI-EMPIRICAL MODEL OF STRAIN SENSITIVITY FOR 4D SEISMIC INTERPRETATION

Colin MacBeth*, Asiya Kudarova[&] and Paul Hatchell[+]

*Heriot-Watt University
Riccarton Campus, Edinburgh, UK
EH14 4AS

[+] Shell Global Solutions International B.V.,
1031HW Grasweg 31,
Amsterdam, The Netherlands

[&] Shell International Exploration and Production,
3333 Highway 6 South,
Houston TX 77082 US

SUMMARY

We reformulate the original model of Hatchell and Bourne (2005) and Røste, Stovas and Landrø (2005) that couples fractional velocity change to subsurface strain via a fundamental constant R. The new model combines elastic compressibility of a dual porosity system for a sand-shale mixture with horizontal planes of inter-granular weakness. The majority of observed R-factor magnitudes from post-stack 4D seismic data in both the reservoir and overburden can thus be explained. R is predicted to depend strongly on lithology and also initial strain state. The model is also extended to predict the observed angle-dependence of time-lapse time-shifts from pre-stack data. An expression for the gradient of time-shift with incidence angle is obtained in terms of the background V_P/V_S, and also the ratio of tangential to normal compliance B_T/B_N representing loss or creation of inter-granular coupling. If accurately estimated from data, this compliance ratio can be used as an additional parameter to assess the post-production state of the overburden. It is concluded that whilst R remains the over-arching parameter controlling the magnitude of time-shifts measured from 4D seismic data, B_T/B_N is a subtler parameter that may also prove of future value.

INTRODUCTION

Production and recovery of oil volumes from hydrocarbon reservoirs naturally generate strain in both the reservoir and surrounding rocks, and these may also manifest as a visible surface subsidence. Thus, for example, hydrocarbon depletion with inadequate pressure support will lead to reservoir compaction (loading of the reservoir rocks) and a corresponding extension of the overburden and underburden (unloading of the surrounding rocks). These geomechanical responses can, under unfavourable circumstances, result in effects detrimental to production such as sanding, well failures, and excessive elevation changes in surface facilities (Doornhof *et al*. 2006). The geomechanical model forms an essential tool for understanding and mitigating the risks posed by these deformations. Necessary input to the calibration process for this model are data from sensitive tiltmeters measuring surface movement (Davis *et al.* 2000), satellite imaging via interferometric SAR images on land (Raikes *et al.* 2008), radioactive bullets or gamma ray correlation downhole (Barkved *et al*. 2003), seafloor or water pressure sensors (Dunn *et al.* 2016), or by time-lapse (4D) seismic surveys. It is the latter surveys that are the subject of this current study, and in particular the interpretation of the time-lapse time-shifts caused by velocity changes induced by the strain.

Time-shifts form a primary source of indirect spatial information on the geomechanical effects, and hence are of importance when helping to quantitatively constrain the sub-surface model. They are measured between time-lapsed seismic datasets that have been migrated using a common (baseline) velocity model (see Figure 1). It has been clearly demonstrated in many previous studies that shifts can be accurately estimated between surveys shot several years apart such as marine towed streamer surveys, or even several months apart using permanent reservoir monitoring. Time-shifts in the overburden due to geomechanical effects were first

observed by Hall *et al.* (2002) for the Valhall field and Hatchell *et al.* (2003) for a depleting gas field in the North Sea. The approach has now gained widespread popularity, and measurements of time-shifts in 4D seismic data associated with moderate to strong geomechanical effects in the overburden, reservoir, and also the underburden, appear now to be universally observed for many types of producing reservoir. From the results of the multitude of field data studies now available, it is possible to draw a common and comprehensive list of key conclusions that may help identify the nature of the phenomenon that connects physical strain to the seismic velocity changes inducing the time-shifts observed in the data.

Key conclusions from vertical time-shifts observed in 4D seismic data

Figure 2 shows a range of published vertical time-shift measurements for overburden and reservoir rocks, in clastic, chalk, and hard-rock carbonate (limestone) fields. The collection is representative but not wholly exhaustive of the available published data. Table 1 provides more details of the individual reservoir depths and thicknesses, and the time periods over which these measurements are made. The majority of time-shifts shown have been measured on stacked migrated data predominantly using the methods of cross-correlation (Hodgson 2009) or non-linear inversion (Rickett *et al.* 2007), and these are typically applied on a trace-by-trace basis. The values reported are the maximum observed over the interval being considered, whether this is the overburden or reservoir. Seismic acquisition is mainly from offshore towed streamer systems, although some specific examples with short repeat period from permanent reservoir monitoring or node-based systems have been published (such as Valhall and Ekofisk offshore, and Peace River onshore). Although most of the reservoirs in these case studies are normally pressured, there are several high-pressure high-temperature examples (Elgin, Franklin, Shearwater).

4

There are four regions of interest in Figure 2 – these correspond to the time-shifts measured during compaction or extension of either the reservoir or overburden. The reservoir signals are less certain because the strain-related signals (relative change in vertical velocity $\Delta V/V$ and physical strain) combine with saturation change signals - these are difficult to separate, particularly for the case of gas saturation. The most noticeable feature of the time-shift estimates is the prominence of slowdown (velocity decrease) due to extension in the overburden as a consequence of reservoir depletion and also due to reservoir inflation (pressuring up by fluid injection). For these effects, the values tend to be large, ranging from 2ms in deep (> 3km) reservoirs over short production/injection time periods of several months - see, for example, Curlew-D (Fehmers *et al.* 2007) and Skua (Staples *et al.* 2007), to more dramatic effects (> 20ms) for compacting chalks such as in the Valhall field (Barkved *et al.* 2003) or Ekofisk field (Janssen, Smith and Byerley 2007) over a period of several years. Indeed, some of the largest reported signals of overburden extension are for the high porosity compacting chalk reservoirs of the North Sea, although many unconsolidated clastics such as in the Genesis field, Gulf of Mexico also exhibit well-developed overburden time-shifts (Hodgson *et al.* 2007).

In contrast, time-shift signals associated with compaction in the overburden or reservoir are less frequently observed. In principle, a compaction response in the overburden is anticipated to be present above active injectors or within the pattern of deformation created by the phenomenon of stress-arching (Røste, Dybvik and Søreide 2015). Reservoir-related speedups are expected to be less easily observed as these changes make targets appear thinner in time and their signal is more difficult to measure. Time-shift values for speedup tend to be small, lying in the range 0.3 to 3ms. This is true even in thick and well-developed intervals of

depletion found in gas reservoirs in regions such as the Southern Gas Basin (MacBeth, Stammeijer and Omerod 2006; Brain *et al*. 2017). However, in these fields the time-shifts are noisier due to imaging difficulties and residual multiple energy from the overlying Zechstein carbonate sequence. Further details on published time-shifts and a description of their origin can be found in the review of MacBeth, Mangriotis and Amini (2018).

In addition to the above observations, a number of general conclusions can be drawn from the extensive published literature available on observed data studied internally by the authors of this paper. These relate to the nature of the phenomenon generating the subsurface time-shifts induced by geomechanical effects, and hence lay the foundation for building a model to understand the behaviour. These statements are ranked below according to prominence:

I.   *Slowdown due to extension is more generally observed in the overburden and reservoir than speedup due to compaction*. In the time-shifts measured from 4D seismic data there appears to be an over-abundance of slowdowns and less frequent occurrence of speedups. Geomechanical simulations do not predict this observational asymmetry.

II.   *Speedup is rarely observed at stress arches or above injectors* - the observation of stress arches also ties into the previous statement. Stress arching should be most noticeable for regions of the reservoir where the area of depletion is spatially confined. Compaction is predicted to exist at the sides of the stress arch, and thus sideburden speedups should be also seen. Observations show that this compaction effect is hard to detect in the seismic data, but extension is always more readily visible (Røste *et al*. 2015; Rodriguez-Herrera *et al*. 2015). In addition, speedup is predicted to

occur above water or gas injectors that inflate pressure in the reservoir – this is rarely observed.

III. *Seismic velocity changes induced by geomechanical effects relate to whole volumes of rock and spread across many varied lithologies* – 'time-strains' appear pervasive and distributed across large volumes of rock in the subsurface, and are therefore not confined to discrete interfaces or subsurface features. Indeed, the strain signals are long wavelength observations and appear to mimic the character of the modelled strain due to production.

IV. *Observations display hysteresis* – time-shifts are associated with pressurised compartments that may or may not diminish during pressure relaxation (Floricich 2006). Evidence for hysteresis also comes from the laboratory (Holt and Stenebråten 2013). However, Røste and Ke (2017) show a complete return with pressure. Surface wave data show speedups in compressional zones only where previous extension took place.

V. *Time-shift variations with offset appear difficult to rationalise* - consideration has been given to the possibility of offset/angle dependent time-shifts (Landrø and Stammeijer 2004) as an additional source of information. Several datasets have shown that time-shifts may, or may not, vary with offset or azimuth (for example, Hawkins 2008, Røste, Landrø and Hatchell 2007; Kudarova *et al.* 2016). Currently, there is no consensus on the expected trend or value of measured pre-stack time-shifts.

VI. *Strong shear-wave birefringence and surface wave anisotropy* - observations for shear waves are limited, however, strong shear-wave birefringence is observed in the

7

shallowest layers at flanks of field where extension is known to take place (Barkved *et al*. 2003; Olofsson *et al*. 2003). Such changes are an order of magnitude larger than in the P-wave data. Scholte waves (dispersive interface waves travelling along the liquid-solid boundary) are also shown to be sensitive to production-induced strains and exhibit an anisotropic behaviour (Hatchell, Willis and Didraga 2009; Kazinnik *et al*. 2014). These waves sample the seabed sediment to depths of 100 to 200m.

VII.   *Microseismic events occur in response to extension and compression* – there are many published examples of microseismic events occurring when the subsurface is extended or compacted in response to production. These small magnitude events may be distributed along faults or lines of weakness, but also distributed throughout the volume of rock (van Gestel *et al*. 2008).

The above statements point towards the mechanisms governing the behaviour of the subsurface rock volume changes, under the action of strain. They suggest that the velocity changes due to strain are pervasive, asymmetric with respect to the polarity of the mechanical response – i.e., larger slowdown response than speedup for the same strain magnitude, and may not vary significantly with azimuth or offset. The microseismic observations also indicate an inelastic response to the mechanical deformation even for quite small strains. In this study, we will attempt to honour the statements listed above by constructing a micro-structural model that connects the production-induced strain to the seismic velocity changes, and hence, to the magnitude and angle dependence of this time-shift phenomenon.

Seismic data analysis and the empirical *R*-factor

The time-shifts observed in 4D seismic data are defined as the difference in two-way time, ΔT, between a common 'event' or trace feature identified on both the baseline and monitor surveys. For post-stack seismic data, the vertical time-shift written in terms of two-way time, t, is given by

$$\Delta T = \int_0^T \left(\Delta \varepsilon_{zz} - \frac{\Delta V}{V} \right) dt , \qquad (1)$$

where ΔV is the change in vertical velocity, V, and T is the time to the event of interest on the baseline seismic data. Thus, the fractional change in two-way time, ΔT, is expressed by the competing effects of elongation/shortening of the propagation path and the fractional velocity changes that slow down/speed up the waves. Key to using this relation is a physical model that links the velocity change to the vertical strain, ε_{zz}. For this, the empirical equation proposed simultaneously by both Hatchell and Bourne (2005) and Røste, Stovas and Landrø (2005) is widely used

$$\frac{\Delta V}{V} = -R \varepsilon_{ZZ}. \qquad (2)$$

Values of *R* are positive, such that positive (extensional) strains give rise to a velocity decrease. The benefits of the Hatchell-Bourne-Røste (*HBR)* model are that it is intuitive, and immediately unites the geomechanical and seismic domains. Thus, the relation may be used when modelling time-shifts from the strains output by geomechanical simulation or for transforming time-shifts measured from the seismic data to vertical strains, ε_{zz}, to provide the required constraints for geomechanical modelling. Hatchell and Bourne (2005) reported that equation (2) matched the

observed time-shifts for four field datasets (a North Sea chalk, a North Sea *HPHT* field, and two further clastic fields), when comparing time-shifts modelled from the geomechanical simulator with measured time-shifts evaluated using cross-correlation. A constant magnitude for the *R*-factor of approximately 5 for the whole overburden was found to replicate the results adequately, suggesting a weak variability of *R* with lithology and geological setting.

Since the early studies of a decade ago, many additional *R*-values have been calculated for a range of fields by various authors. Many published *R*-values for the *HBR* model are now available for a range of fields, both for the compacting reservoir R_{res}^- and the overburden in extension R_{ob}^+ (where the superscript '-' refers to compression, and '+' to extension). Table 1 provides a list of overburden and reservoir *R-factor*s obtained from field studies published in open literature prior to and including 2017. Note that these values are averages for the overburden and reservoir, and do not split the observations into individual zones. There are several categories of estimate, based on the robustness of the estimation procedure. Those values for which we have the largest confidence are calculated from well-determined subsurface strain data and highly repeatable time-lapse seismic data. Strain is well determined if the simulation predictions are calibrated via core data, seafloor subsidence records, gravimetric data, direct measurement underneath the platform, or radioactive bullets. Onshore, satellite imaging of the subsidence can also be employed together with tiltmeters. Three such well-calibrated examples exist for Valhall, Ekofisk and Mars (Hatchell, Kawar and Savitski 2005; Janssen et al. 2007; Hatchell and Bourne 2005), and indicate R_{ob}^+ values that lie between 4 and 9, and R_{res}^- values of less than 2. Estimates extracted from data using unconstrained geomechanical modelling or techniques such as the Geertsma modelling (Geertsma 1973) of Wong and MacBeth (2016) must be regarded with less confidence. Nevertheless, these estimates show a similar range of relative magnitudes. In general, published data indicate R_{ob}^+

values lying between 4 and 35, whilst R_{res}^{-} values are typically a factor of 3 lower. Most measurements occupy a narrow range despite the varied field settings and lithologies sampled. Occasional outliers are recorded with R_{ob}^{+} values as high as 100, in addition to an unexplained R_{ob}^{+} of -1 in a Malaysian field (Shell, private communication). For this latter case, explanations of a fluid origin or physical displacement were sought but discounted. Finally, it is noted that R_{ob}^{-} and R_{res}^{+} are rarely reported from field data studies – indeed it is assumed naively that R_{ob}^{-} = R_{res}^{-} and R_{ob}^{+} = R_{res}^{+}.

The time-shift observations in Figure 2 can be related directly back to the *HBR* model as a practical cross-check. This requires knowledge of the magnitude of subsurface strain induced by reservoir production and recovery. Geomechanical simulation provides one route to this understanding, and the published literature provides many direct measurements of strain. For example, the during many years of production, the Ekofisk field compacted by 30cm per year to give 6m of subsidence over a 2500m thick overburden; the Valhall field exhibited a compaction rate of 20cm a year to give a subsidence of 5.6m over a 2400m thick overburden; the Groningen gas field displayed 25 cm subsidence at 3km depth; and in Matagorda Island, Gulf of Mexico, poorly consolidated sands exhibited a subsidence bowl of about 30cm (1ft) at depths of about 3048m (10,000ft) (Doornhof *et al.* 2006). Such observations conform to approximate overburden strains of between 10^{-3} and 10^{-4}, with those in the reservoir roughly an order of magnitude higher. Thus an *R-factor* of 2 for compaction could lead to a maximum time-shift developed over a 100ms interval (such as a thick reservoir) of 2ms, whilst an *R-factor* of 5 for extension gives a time-shift of 10ms developed over a 2000ms overburden (corresponding to velocity changes of 2% and 0.5%, respectively). In contrast, extension in the reservoir and compaction in the overburden, give time-shifts of 5ms and 4ms. These ballpark

levels are marked on Figure 2, and are seen to mostly agree with the observations, despite the variability of field setting and measurement intervals.

In the laboratory, there have been numerous historical experiments on extracted core samples detailing rock stress sensitivity stretching back to Nur and Simmons (1969). However, there are only a limited number of studies that report the explicit behaviour with strain (see the value range drawn in Table 2). In this latter group of publications, some clear dependent variables emerge and some overall qualitative trends can be obtained. It is concluded that R strongly depends on the initial stress state and stress path (hydrostatic loading producing larger values than uniaxial loading). R decreases with increasing stress, varies with lithology and decreases with water saturation (by a factor of about 2). Tests on unconsolidated samples indicate that near the onset of plasticity (grain-grain crushing and sliding), R-values decrease to zero or are negative. In general, laboratory values tend to be much larger than field observations, if core samples contain internal microfractures and cracks. The condition $R^+ > R^-$ is also tested and confirmed in several laboratory studies as being independent of lithology. Holt, Nes and Fjaer (2005), Holt *et al.* (2008), and Holt and Stenebraten (2013) describe a comprehensive set of experiments that measure R-factors for uniaxial and hydrostatic loading of artificial materials (for example, uncemented beads), synthetic sandstone and claystone, unconsolidated sands, and field core samples of sandstone and shale. Their values generally agree with field values, although some tend to be higher. The exception to this is a synthetic sandstone, for which R is measured under unloading as 75, whilst loading gives 15, but unloading after loading is 55. Similarly, Janssen *et al.* (2007) observed values of 10 to 30 for Ekofisk chalk in the laboratory (as opposed to 2 to 6 in the 4D seismic data). Bathija, Batzle and Prasad (2009) measured three sandstones and one shale

sample under hydrostatic and uniaxial loading, and found R-factors of between 6 and 91 for the sandstones and 6 to 11 for the shales. Also this publication provides R-values calculated from the data of Sarkar, Bakulin and Kranz (2003), Vega (2003), and Wang (2002) – all values are much higher than those reported elsewhere.

Whilst the empirical *HBR* model appears robust and capable of predicting the majority of our observations to date, there are a number of questions that have not been addressed in the literature:

(a) An underlying physical model to explain the origin of the R-factor and its possible relation to lithology is unclear – such a description is important to enhance the predictive capability of the model;

(b) Accurate relative values for the four possible factors R_{ob}^{+}, R_{res}^{+}, R_{ob}^{-}, and R_{res}^{-} still requires investigation;

(c) The general applicability of the *HBR* model beyond vertical wave propagation is still under dispute (see, for example, Kudarova *et al.* 2016);

(d) In the *HBR* model only the vertical strain is used and not the full strain tensor – this may inherently limit the usefulness of the observed time-lapse data;

(e) The velocity changes are currently assumed to be isotropic, despite mathematical predictions, geomechanical and laboratory studies, and intuition suggesting otherwise.

The purpose of this current study is to address the above criticisms (a) to (e), and to extend the *HBR* model to fit the context provided by observations (I) to (VII) outlined in the previous section. In the following sections a pragmatic model is developed which attempts to address these observations and as a starting point based on the original conceptual understanding of Hatchell and Bourne (2005). The next section will describe the development of a model for

velocity change based on two elements: firstly, the compressibility of the rock pore volume which we consider to be a sand-shale system with dual-porosity; and secondly, multiple planes of granular weakness created by the geomechanical deformations. It will then be seen how this model can be used to explain offset or angular dependent velocity change and hence time-shift variation.

SEISMIC VELOCITY CHANGE
INDUCED BY ROCK DEFORMATION

In this current study we seek to reconcile the observations (I) to (VII) listed in the previous section and resolve the issues in (a) to (e) above, using a model that aligns closely with the empirically-driven *HBR* model. We generalise to offset/angle dependence to provide an understanding of the physics behind the *R*-factor for the benefit of reservoir interpretation. Before doing this, we firstly review current literature on the topic of velocity change induced by subsurface strain, for which some development and explanations have already been provided.

There are several schools of thought regarding the appropriate physics to describe the velocity-strain dependence. One of the most popularized originates from acoustoelastic theory (Murnaghan 1937; Landau and Lifshitz 1986), where third order coefficients are introduced to describe a nonlinear relation between stress and strain (the coefficients in the expansion of the strain energy function up to the third order in strain). Prioul, Bakulin and Bakulin (2004) used this theory to capture the behaviour of the full anisotropic elastic tensor in response to applied anisotropic stresses/strains. The principal motivation behind this approach was to better understand the effect of anisotropic stresses on the shear-wave or angle-dependent *P*-wave propagation. Here it is recognised that uniaxial deformation creates transverse isotropy with a vertical symmetry axis, for which three independent nonlinearity parameters are required in addition to the five linear elasticity VTI parameters to define the wave properties. Prioul *et al.* (2004) invert for these three coefficients from laboratory datasets: a Jurassic North Sea shale undergoing hydrostatic loading and Colton sandstone under biaxial loading with equal

horizontal stresses. The proposed theory is believed to be sufficiently general to act as a macro-model description for a wide range micro-structural mechanisms of deformation such as grain stiffening and fracture closure. However, in its original form, it is too general for practical use in 4D seismic interpretation. As a step towards simplification, Herwanger (2008) presented an equation from the third order elasticity approach that connects the change in vertical strain ε_{zz} and horizontal strain ε_{xx} and ε_{yy}, to the vertical velocity, V, via two independent 3$^{\text{rd}}$ order coefficients, c_{111} and c_{112},

$$\frac{\Delta V}{V} = \frac{1}{2}\frac{c_{111}\varepsilon_{zz} + c_{112}(\varepsilon_{xx} + \varepsilon_{yy})}{C_{33}},$$

(3)

where C_{33} is the vertical component of the pre-production elastic stiffness tensor such that $V = \sqrt{C_{33}/\rho}$, where ρ is the density. Using numerical modelling, Herwanger (2008) concludes that the observation $R_{ob}^{+} > R_{res}^{-}$ can be explained by this equation. For zero overall volumetric changes such that $\varepsilon_{xx}+\varepsilon_{yy}+\varepsilon_{zz} = 0$ (expected to be approximately the case for the overburden, provided there are no mechanical contrasts, structural dip and there is linear elasticity), $R = -1/2[(c_{111} - c_{112})/C_{33}]$. For a uniaxial condition, in which lateral strain is zero (believed to be similar to the reservoir state), $R = -1/2[c_{111}/C_{33}]$. Substituting the coefficients from the laboratory study of Prioul *et al.* (2004), yields $R_{ob}^{+} = 51$ and $R_{res}^{-} = 38$. Rodriguez-Herrera *et al.* (2015) continues this theme by proposing a strain sensitivity model with two polarity-insensitive *R*-factor parameters, R_1 and R_2 (similar to those suggested by Fuck, Bakulin and Tsvankin 2007). This is believed to extend the *HBR* model to a generalised principal strain tensor:

$$\frac{\Delta V}{V} = -R_1 \varepsilon_{zz} - R_2 (\varepsilon_{vol} - \varepsilon_{zz}), \tag{4}$$

where ε_{vol} is the volumetric strain, and $R_1 = -1/2\,(c_{111}/C_{33})$ and $R_2 = -1/2\,(c_{112}/C_{33})$. These factors relate respectively to components parallel and perpendicular to the wave propagation direction. Using the Prioul *et al.* (2004) data, R_1=51 and R_2=45. These proposed models collapse to the *HBR* model under conditions of zero volumetric strain, hydrostatic loading, and uniaxial loading. Finally, Rodriguez-Herrera *et al.* (2015) perform numerical calculation of the time-shifts for a field case study involving stress arching and employing the full tensor strain output from a geomechanical simulation with a favourable comparison to field data. However, to make practical use of equation (4), the laboratory-derived coefficients R_1 and R_2 must be fully calibrated to the field study observations.

Although the *R*-factor is linked directly to the third-order coefficients in some work, it is important to understand that the third-order coefficients are the intrinsic elastic properties of a material, while the *R*-factor, as introduced by Hatchell and Bourne (2005), is stress-dependent. It has been noted by Holt *et al.* (2005) that the *R*-factor depends not only on rock properties, but also on local stress geometry and it can vary laterally in the field even if the rock properties are uniform. Obtaining an *R*-factor from laboratory tests is therefore difficult and a direct relation between the *R*-factor and the third-order coefficients is not appropriate. This may be the reason for discrepancies in the *R*-factor values estimated with the use of third-order coefficients, and the strong offset dependence predicted by the models which employ these coefficients (for example, Fuck, Bakulin and Tsvankin 2009).

A separate school of thought from the above considers instead of the full anisotropic tensor a specific micro-structural model for the subsurface rocks. Sayers (2006) employs such a model to explain the observation $R_{ob}^+ > R_{res}^-$ from reservoir depletion. His underlying model assumes stress-sensitive grain-grain contacts that vary their contact weakness exponentially according to the applied normal stress at their boundaries. This inter-granular compliance function is sufficient to explain the observed extension-compaction asymmetry in addition to the non-linear variation of velocity with stress. He also notes that the impact of stress path will exaggerate the asymmetry. Two further micro-model estimates for *R* have been considered by Carcione *et al.* (2007), who developed an expression based on the 'bed of nails' asperity distribution which gave an *R* of between 3 and 5 both for hydrostatic and uniaxial deformation. He also considered the popular Hertz-Mindlin contact theory for a spherical grain pack, which gave similar values of between 2 and 5.

The above models satisfy points (d) and (e) above (although clearly in the formal sense this does not mean they describe the physics and the anisotropy in the right manner). They also address the observations *I*, *II* and *III*. However some points still remain - these require an understanding of how sedimentary rocks deform under the stresses created by production and recovery. An overarching model that satisfies the remaining requirements, and combines the benefits of both 3rd order theory and the compliance model, can be found by re-considering the original conceptual model of Hatchell and Bourne (2005). The underlying basis for this will now be discussed below.

Micromechanical deformation of rocks

Key to our understanding of rock deformation is the behaviour of sedimentary rocks under applied stress. Subsurface sedimentary rocks contain a fabric of grains of varied mineralogy, bonded by differing proportions of carbonate cements, clays or pressure solution, depending on diagenetic history (Pettijohn, Potter and Siever 1987). At the depths relevant to most hydrocarbon production activities, the grains are relatively incompressible and strongly resistant to applied stress, whilst the cements and clays are variable in weakness. As a rock is compressed, it initially responds elastically to small strains by stiffening contacts and decreasing pore volume. However, as strains increase, the rock fails at grain-grain contacts, and at progressively higher loads due to sliding, rotation and breakage of grains. Jones *et al.* (1992) suggest that the elastic limit for compaction may be as small as a few millistrains, particularly for unconsolidated or over-pressured sandstones – which is similar to those strains encountered in the inter-well space during production. The observation of microseismic activity (item *VII* above) also suggests small-scale internal damage occurs.

For reservoir compaction, a general velocity change is given by:

$$\Delta V_{res} = \left[\Delta V_{pv}\right]\uparrow + \left[\Delta V_{cs}\right]\uparrow + \left[\Delta V_{cw}\right]\downarrow, \tag{5}$$

where ΔV_{pv} is the increase ($\uparrow$) due to the pore volume reduction, ΔV_{cs} the increase due to contact stiffening, and ΔV_{cw} a decrease ($\downarrow$) from contact or pore space damage. The balance of these contributions depends on the rate of depletion, the lithology, degree of overpressure and initial stress state. For extensional strains in the overburden, pore volume increases may be small except in regions where net volumetric strain is significant. Irreversible failure of inter-granular cement bonds is expected to be the dominant mechanism as rocks are known to be an

19

order of magnitude weaker in extension than compression (Holt *et al*. 2005). This mechanism may dominate despite the subsurface being in an initial static state of compression. In the case of extension, the velocity change is therefore given by:

$$\Delta V_{ob} = \left[\Delta V_{pv}\right]\downarrow + \left[\Delta V_{cw}\right]\downarrow, \qquad (6)$$

where ΔV_{pv} refers to the decrease due to pore volume inflation, and ΔV_{cw} that due to contact detachment. Here, the velocity changes act together to enhance the response and an overall reduction in velocity is guaranteed. Inelastic mechanisms for the response to both compaction and extension may also explain some of the evident hysteresis in observation *IV* above – this has also been observed in the laboratory (Holt and Stenebråten 2013). Clearly, the mechanisms for extension and compaction will be observed particularly strongly in shear wave data – as indicated in observation *VI*.

To quantify the velocity change for the individual mechanisms, we initially follow the conceptual model of Hatchell and Bourne (2005) and determine the relationship to the strain change. The focus on strain (rather than stress) is preferred because in practice it removes the need to involve compressibilities and stress-strain relations in the link to the seismic observations. It is also easier to relate to the geomechanical consequences of the reservoir production, and also more intuitive. According to Hatchell and Bourne (2005) and the above description there are two main components of velocity change to consider: the contributions from: (i) pore volume changes and; (ii) inter-granular bonds (breakage or creation). These are discussed separately in the sections below.

Velocity changes due to the pore volume compressibility or expansion

Consider first the control on seismic velocity from mechanically induced changes of pore volume alone (due to change of external stresses or pore pressure). We assume that the pore space exhibits no preferential alignment as a consequence of the strain, such that the rock properties and their changes may be considered isotropic. Clearly, this assumption is not valid for rocks such as shales, for which the following will, instead, be an approximation. Also assumed is that the deformation is not influenced by contributions from the cements and clays in the rock. The fractional change in velocity $\dfrac{\Delta V}{V}$ generated predominantly by small volumetric strain is:

$$\frac{\Delta V}{V} = \frac{1}{V}\frac{dV}{d\varepsilon_{vol}}\varepsilon_{vol} \, , \tag{7}$$

where ε_{vol} is the bulk volumetric strain as before, with positive strain defined as rock dilation. Assuming the strain is fully accommodated by a change of pore volume, but no change in pore shape, equation (7) can be re-written in terms of porosity,

$$\frac{\Delta V}{V} = \frac{1}{V}\left[\frac{\partial V}{\partial \Phi}\frac{\Delta \Phi}{\varepsilon_{vol}}\right]\varepsilon_{vol}, \tag{8}$$

from which the *R-factor* may be derived by definition. The relationship between measured volumetric strain and porosity change, $\Delta\Phi$, depends upon whether mechanical deformation has

taken place under drained or undrained conditions. The rock response is drained if fluids flow freely out of the pore space upon application of applied stress, and thus pore pressure is constant. However, for undrained conditions, fluid does not flow into or out of the pore space, and, hence, in this case a change in pore pressure will be induced. In the undrained case, the volumetric strain is smaller for any given applied stress than for the drained case. Over the time period of deformations caused by fluid production or injection (hours or days), loading may be considered slow enough to lead to a drained response for clean permeable sandstones. For shales with permeability of only a few millidarcies, the undrained response is more applicable. For the drained response, the change of porosity depends on strain, initial porosity, and the Biot-Willis coefficient α (Schutjens *et al.* 2004):

$$\Delta\Phi = \frac{\varepsilon_{vol}}{1+\varepsilon_{vol}}(\alpha - \Phi) \approx \varepsilon_{vol}(\alpha - \Phi), \tag{9a}$$

where $\alpha = 1 - C_r/C_{bc}$, and C_r is the grain compressibility and C_{bc} the bulk compressibility. Note the sign change in the denominator from Schutjens *et al.* (2004) to take care of our definition of sign for strain. The approximation is accurate for the small values of strain (10^{-3}) observed in our field cases; that is, $\Delta\Phi$ up to 0.1%. When the grains can be considered incompressible or insignificant, α is unity – this is the situation for unconsolidated sediments. However, α tends towards much lower values for consolidated rocks with more rigid skeletons such as strongly cemented sandstones. For the undrained case, the change of porosity is linked to strain via a function, F, of porosity, fluid compressibility, C_f, and bulk compressibility, C_{bc}. For the general case, calculations based on Zimmerman (1991) show that

$$\Delta\Phi = \frac{\varepsilon_{vol}}{1+\varepsilon_{vol}} F(\Phi, C_f, C_{bc}) \approx \varepsilon_{vol} F(\Phi, C_f, C_{bc}) \,. \tag{9b}$$

For the specific case of incompressible grains, then $F \approx (1-\Phi)$, and equation (9b) is identical to equation (9a) when $\alpha = 1$. In the case of a fluid compressibility much greater than the bulk rock compressibility, then $F \approx (\alpha - \Phi)$, and equation (9b) is identical to (9a). An example of a saturated rock in the latter condition is shown by Zimmerman (1991) for which the compressibility of water is 4×10^{-4} MPa^{-1} whilst the low porosity Fort Union sandstone has a bulk rock compressibility of 0.286×10^{-4} MPa^{-1}. To generalise the development to follow for the drained and undrained case, we choose to work with equation (9a) and $\alpha = 1$, but understand that if these assumptions are not fulfilled, the resultant R-factor will deviate from our predictions. Combining equations (8) and (9a), and inspection of equation (2), yields an equation for the R-factor based on the sensitivity of the velocity to pore size for constant pore shape alone. The relevant R-factor, R_A, defined for the vertical velocity V can now be written:

$$R_A = -\frac{(\varepsilon_{vol}/\varepsilon_{zz})}{V}\left(\frac{\partial V}{\partial \Phi}\right)(1-\Phi). \tag{10}$$

Given our observation of a negative R in Table 1, it is interesting to note that for the drained case, if $\alpha < \Phi$, then R_A does indeed become negative. It should also be noted that these calculations predict that $R_A^+ = R_A^-$, provided the stress paths for compression and elongation are exactly replicated. For a predominantly uniaxial strain in the reservoir, the ratio, $\varepsilon_{vol}/\varepsilon_{zz}$, is

close to unity and the expression in Hatchell and Bourne (2005) is recovered. For the overburden, the net volumetric strain may be close to zero, provided there are no strong mechanical contrasts between the reservoir and the overburden. Hence, the *R-factor* from the compressibility mechanism is small. In practice, $\varepsilon_{vol}/\varepsilon_{zz}$, will be a function of the local stress geometry, and may therefore vary with position (Holt *et al*. 2005).

The term $\partial V/\partial \Phi$ in equation (8) expresses the sensitivity of the vertical velocity to small changes in porosity. In practice, this depends on the initial stress state, lithology, cements, clays, pore volume geometry and porosity. As velocity usually decreases with increasing porosity, the resultant *R*-factors in equation (10) are therefore positive. A multitude of velocity-porosity relations exist in the literature from empirical trends derived by regression fit of analytic equations to laboratory or wireline log data (for example, see Mavko, Mukerji and Dvorkin 2009). Hatchell and Bourne (2005) calculated *R*-factors for a selection of such trends and determined that values must lie between 1 and 3. Assuming a uniaxial stress path and taking a selection of well-known laboratory–derived linear relations between porosity and velocity, Røste *et al.* (2015) similarly concluded that *R* is 1.5 for chalk, 1.6 to 2.4 for sand, and 2.7 to 3.6 for clay. However such empirically-driven velocity-porosity trends do not properly capture the sensitivity of velocity to porosity changes directly induced by strain in the producing reservoir, as the empirical variations they capture are ostensibly lithological in origin. For an alternative approach we use a velocity-porosity relation derived from a model for which lithology can be held constant, whilst porosity can be reduced. The popular inclusion-based model of Xu and White (1995) is chosen as it is known to accurately predict velocity in shaley sand formations. In this approach, the pore volume is built from two sets of oblate spheroidal inclusions: one set is the stiff sand-related pores, and the other the more compliant shale-related pores. The proportion of each set of pores is determined by the measured volume

24

of shale. To compute the porosity sensitivity of velocity we firstly calculate the dry rock bulk

modulus, κ_{dry}, and shear modulus, μ_{dry}, using the Keys and Xu (2002) dry rock approximation

for the Xu-White model:

$$\kappa_{dry} = \kappa_0 (1 - \Phi)^p \tag{11}$$

and

$$\mu_{dry} = \mu_0 (1 - \Phi)^q \tag{12}$$

where p and q are known functions of the sand and shale-related pore aspect ratios α_{sa} and α_{cl}

respectively, and κ_0 and μ_0 are the grain modulus,. These functions are valid up to the critical

porosity, which is determined according to $\Phi_{crit} = 1/p$ for equation (11) and $\Phi_{crit} = 1/q$ for

equation (12). Next, we saturate the dry rock frame using Gassmann's equation (Mavko *et al.*

2009) to determine κ_{sat} and ρ_{sat}, and hence derive V. This permits a calculation of the R_A factor

for pore size change alone as $\partial V / \partial \Phi$ is readily computed numerically.

Another benefit of the dual-porosity Xu-White model is that a change of pore space shape can

also be taken into account. Thus, instead of reducing the pores by size, the porosity can also be

varied by changing the aspect ratio in response to stress. The change in velocity with porosity

can now be written according to the chain rule:

$$\frac{\partial V}{\partial \Phi} = \frac{\partial V}{\partial \alpha_{sa}}\frac{\partial \alpha_{sa}}{\partial \Phi} + \frac{\partial V}{\partial \alpha_{cl}}\frac{\partial \alpha_{cl}}{\partial \Phi} \tag{13}$$

from which the *R-factor* determined for aspect-ratio change alone may be written:

$$R_B = \left(\frac{\partial V}{\partial \alpha_{sa}}\frac{\alpha_{sa}}{\Phi} + \frac{\partial V}{\partial \alpha_{cl}}\frac{\alpha_{cl}}{\Phi} \right)(1 - \Phi), \tag{14}$$

as the fractional change in the mean aspect ratio is determined to be proportional to the fractional change in porosity, scaled by strain. In practice, the partial differentials are determined numerically for any particular pair of aspect ratios.

The resultant R_A (pore size changes only) and R_B (aspect ratio changes only) factors for two different sand and shale-related aspect ratios are shown in Table 3(a), and as a function of porosity and shale content in Figures 4 and 5 respectively. The *R*-factors are determined (and defined) for a uniaxial strain path only, and therefore represent an upper limit on the possible values. Aspect ratios are chosen to represent the extremes of the accepted distribution from the literature, for which sand-related pores lie in the range 0.15 to 0.27 and shale-related pores are calculated to be between 0.02 to 0.04 (see, for example, Keys and Xu 2002; Simm and Bacon 2014). Using these typical values, *R*-factors are larger for shaley-sand than for pure sandstone due to the more compliant nature of the shale-related pores. This effect is more pronounced when considering only aspect ratio changes. The effect of 100% brine saturation via Gassmann is to decrease all *R*-factors. This agrees in general with the observations from the laboratory as

discussed above. *R*-values of 1 to 6 are predicted when the porosity change is caused by pore size reduction, but much larger values of 28 to 95 (dry rock frame) and 1 to 30 (brine-saturated rock) are predicted for porosity changes caused by variation of aspect ratio. The Xu-White model is also sufficiently versatile to simulate a range of lithologies. Thus, homogeneous chalks are known to contain a high percentage of stiff pores, and can be modelled by inclusions with aspect ratios close to 0.65 (see also Table 3(a)). Using the Xu-White theory the *R*-factors are predicted to be between 1 and 3 for porosities between 0% and 25% porosity respectively. For carbonates containing fractures, low aspect ratio inclusions ($\alpha = 0.01$) dominate to yield high *R*-factors up to 20.

Comparing the values above with the field and laboratory values in Tables 1 and 2 (also Figure 3), it is clear that the Xu-White model for sand-shales systems, calibrated using an acceptable range of aspect ratios, can simulate the majority of the *R*-factors observed in our data which lie in the range 1 to 30. However there still exist some anomalously large measured values (> 30) from field and laboratory data (see Figure 3). For example, seismic data at Ekofisk and Snorre (compacting chalk and clastic reservoirs) give values for the overburden of 20 (Table 1), but for the HPHT fields of Shearwater and Elgin-Franklin values are between 20 and 100. Our calculations indicate that large *R*-factors can be generated by low aspect ratio pores (or cracks/fractures). In the laboratory, high values of *R* are attributed to contact breakage and micro-fracturing within the rock samples (Holt *et al*. 2005). Such fractures may assume a distribution of preferred alignment for which the Xu-White model in the form presented above is not readily applicable. Thus, to explain this additional set of observations, a model for the damage component must also be developed.

Velocity changes due to contact breakage or creation

We consider the popular excess compliance approach of Sayers (2006) to link inter-granular weakening to velocity change. In this theory, all grain-grain bond weakening (or strengthening) is represented by small planar elements of excess compliance embedded in the rock – variously referred to in publications over the past four decades as 'cracks' (a term that will be preserved here for convenience and succinctness of expression, but with the recognition that cracks per se may not actually be physically present). Firstly, consider the extension scenario described in equation (6) above. As the rock weakens, the population of compliances increases. Following Sayers and Kachanov (1995), the total elastic compliance tensor, S_{ijkl}, of the rock can be written

$$S_{ijkl} = S_{ijkl}^0 + \Delta S_{ijkl} \,, \tag{15}$$

where S_{ijkl}^0 is the compliance at the initial (pre-production) state which we assume to be isotropic, and ΔS_{ijkl} the excess compliance created by the "cracks". The excess compliance term is defined formally by the normal, B_N, and tangential, B_T, compliances for each crack and their three-dimensional orientation angles. Sayers and Kachanov (1995) define an expression for excess compliance:

$$\Delta S_{ijkl} = \frac{1}{V_T} \sum_r \left[\frac{1}{4} B_T \left(\delta_{ik} n_j n_l + \delta_{il} n_j n_k + \delta_{jk} n_i n_l + \delta_{jl} n_i n_k \right) + (B_N - B_T) n_i n_j n_k n_l \right] A_r \tag{16}$$

where the summation is over all r cracks in the volume V_T. Each crack has a cross-sectional area, A_r, the vector $\mathbf{n} = (n_1, n_2, n_3)$ points normal to the crack face, and δ_{ij} is the Kronecker delta. To apply this theory, the orientation of the cracks must be decided. The scenarios most relevant to our reservoir condition can be classified into four possible end-member distributions: horizontal alignment, vertical alignment, isotropic orientation distribution, and cracks with normals distributed randomly within a horizontal plane. Grain-grain bonds may break in the reservoir or overburden along horizontal planes if the extensional stress is uniaxial and vertical. For more general extensional conditions, vertical planes of cracks with normals aligned along the direction of maximum horizontal stress or a more random distribution may prevail. For uniaxial compression, grain-grain contacts may close along horizontal planes but also may be damaged if the load becomes excessive and a random distribution with co-planar normals becomes relevant.

A horizontal distribution of cracks was also considered by Hatchell and Bourne (2005) as an explanation for large R-factors, thus we also consider this distribution. According to Sayers (2006) the relevant stiffness matrix C for the post-production state with horizontal cracks aligned with their normal pointing along the vertical 3-axis is calculated after inversion of the compliance tensor:

$$
C = \begin{pmatrix}
M(1-r^2\delta_N) & \lambda(1-r\delta_N) & \lambda(1-\delta_N) & 0 & 0 & 0 \\
\lambda(1-r\delta_N) & M(1-r^2\delta_N) & \lambda(1-\delta_N) & 0 & 0 & 0 \\
\lambda(1-\delta_N) & \lambda(1-\delta_N) & M(1-\delta_N) & 0 & 0 & 0 \\
0 & 0 & 0 & \mu(1-\delta_T) & 0 & 0 \\
0 & 0 & 0 & 0 & \mu(1-\delta_T) & 0 \\
0 & 0 & 0 & 0 & 0 & \mu
\end{pmatrix}, \qquad (17)
$$

where the isotropic reference state is given by the Lamé parameters, λ and μ, and the parameter $r = \lambda/(\lambda+2\mu)$, and M is the P-wave modulus $(\lambda+2\mu)$. δ_N and δ_T are the reduction in stiffness corresponding to the excess compliance introduced by the elements of weakness. Consider the damage components to be represented by N self-similar cracks per unit volume with a circular cross-section of radius a, and described by B_N and B_T. In this case we can write $\delta_N = N\pi a^2(\lambda+2\mu)B_N$ and $\delta_T = N\pi a^2 \mu B_T$ for small compliances (Sayers and Kachanov 1995). The stiffness matrix in equation (15) has transverse isotropy with a vertical axis of symmetry. For the particular case of vertically propagating P-waves the vertical velocity is $V = \sqrt{C_{33}/\rho}$.

Hence, the desired fractional time-lapse change in velocity, $\dfrac{\Delta V}{V}$, between post and pre-production strain states is given by:

$$\frac{\Delta V}{V} = \frac{V^2(after) - V^2(before)}{2V^2(before)} \approx -\frac{1}{2}\delta_N. \tag{18}$$

Thus, the fractional change in vertical velocity depends, as expected for horizontal cracks, only on the normal compliance of the cracks. To determine the corresponding R-factor, we assume that the cracks are solely responsible for the pore volume change. For N cracks of volume V_C, the overall macroscopic change of porosity, $\Delta\Phi$, is given as NV_C, this giving the volumetric strain, ε_{vol}, from the horizontal cracks as $NV_C/(1-\Phi)$. Thus the number of cracks grows in proportion to the strain change. The fractional velocity change is therefore:

$$\frac{\Delta V}{V} \approx \left[\frac{1}{2V_C}(1-\Phi)\pi a^2(\lambda+2\mu)B_N\right]\varepsilon_{vol}. \tag{19}$$

The specific case of 'dry' oblate spheroidal cracks in a homogeneous isotropic background gives $B_N = 16(1-v^2)a/3\pi E$, where $v = \lambda/2(\lambda+\mu)$ and $E = \mu(3\lambda+2\mu)/(\lambda+\mu)$ are the Poisson's ratio and Young's modulus, respectively, for the initial pre-production state. This solution relates only to 'dry' cracks and the subsurface being fully saturated. However, fluid pressure equilibrates freely between the cracks and the pore volume at seismic frequencies (i.e., no resistance to deformation of the crack shape with the passage of the elastic wave). It is therefore expected that the 'dry' solution for the normal crack compliance may also be applicable, or at least only slightly reduced in the saturated case (Sayers and Kachanov 1995). Inserting $V_C = 4/3\pi a^3\alpha$ for an oblate spheroid gives the final R-factor for this contribution:

$$R_{C1} \approx \frac{1}{\alpha}(1-\Phi)\left[\frac{2(\lambda+2\mu)(1-v^2)}{\pi E}\right]\frac{\varepsilon_{vol}}{\varepsilon_{zz}}, \qquad (20)$$

where α is the ratio of the minor to major axis of each crack. The R-factor is therefore a constant for any particular rock, and a function of porosity and aspect ratio (as in the Xu-White model described earlier). It should be noted that there is a similarity in the background theory between Xu and White (1995) and Sayers and Kachanov (1995), and this explains why both predictions are controlled by aspect ratio. Setting $g = (V_S/V_P)^2$, where V_P is the P-wave velocity and V_S the shear-wave velocity, we observe that $v = (1-2g)/2(1-g)$ and $E = \mu(3-4g)/(1-g)$. Assigning $g = 1/4$ (or $V_P/V_S = 2$) gives $v = 1/3$ and $E/(\lambda+2\mu) = 2/3$, and hence $R_{C1} \approx (1-\Phi)/\alpha$. Values for this crack-related R-factor are tabulated alongside those obtained from the Xu-White model in Table 3(b). For a 25% porosity rock an aspect ratio of 0.001 predicts an R-factor of 750, whilst an aspect ratio of 0.01 predicts an R-factor of 75. There is a strong velocity sensitivity to the very small aspect ratios associated with these 'cracks', and this explains the large R-factors found in the laboratory for micro-fractured samples (Holt *et al*. 2008) or observed in the field

data. The predictions above represent an upper limit on R, as they assume strain is predominantly created by the appearance of 'cracks'. In practice, the pore space and grain contact mechanisms share the strain according to their relative compressibilities and thus values are lower.

For an isotropic orientation distribution of self-similar cracks that grow in number in proportion to the magnitude of the strain, the post-production state is isotropic. In this case, Sayers and Kachanov (1995) yield, after some manipulation, the elastic constant associated with vertical P-wave velocity after production:

$$C_{33} = (\lambda + 2\mu)\left[1 - \frac{1}{15}(\lambda + 2\mu)\left((5\alpha + 9\beta) + 12r\beta + 2r^2(5\alpha + 12\beta)\right)\right] \qquad (21)$$

where $r = \lambda/(\lambda + 2\mu)$ as before, and $\alpha = N\pi a^2 B_T$ and $\beta = N\pi a^2(B_N - B_T)$ for small compliances. Thus, assuming once again, oblate spheroids, $B_T = 32(1 - \nu^2)a/3\pi E(2 - \nu)$, the R-factor can be written as:

$$R_{C2} \approx \frac{1}{\alpha}(1 - \Phi)\left[\frac{(\lambda + 2\mu)}{15}\left((5k_\alpha + 9k_\beta) + 12rk_\beta + 2r^2(5k_\alpha + 12k_\beta)\right)\right]\frac{\varepsilon_{vol}}{\varepsilon_{zz}}, \qquad (22)$$

where $k_\alpha = 8(1 - \nu^2)/E(2 - \nu)$ and $k_\beta = -\frac{4\nu}{2 - \nu}\left((1 - \nu^2)/E\right)$. For cracks with normals randomly distributed in the horizontal plane, the post-production state is transversely isotropic. Again, after some manipulation, Sayers and Kachanov (1995) give the elastic constant associated with the vertical velocity, or:

$$C_{33} = (\lambda + 2\mu)\left[1 - r^2(\lambda + 2\mu)(\alpha + \beta)\right] , \qquad (23)$$

and the relevant *R*-factor becomes:

$$R_{C3} \approx \frac{1}{\alpha}(1 - \Phi)\left[r^2(\lambda + 2\mu)(k_\alpha + k_\beta)\right]\frac{\varepsilon_{vol}}{\varepsilon_{zz}} . \qquad (24)$$

Finally, for the case of vertical cracks oriented with normal along the x_1 axis, the overall stiffness tensor for the post-production state can be obtained from equation (15)

$$C = \begin{pmatrix} M(1-\delta_N) & \lambda(1-\delta_N) & \lambda(1-\delta_N) & 0 & 0 & 0 \\ \lambda(1-\delta_N) & M(1-r^2\delta_N) & \lambda(1-r\delta_N) & 0 & 0 & 0 \\ \lambda(1-\delta_N) & \lambda(1-r\delta_N) & M(1-r^2\delta_N) & 0 & 0 & 0 \\ 0 & 0 & 0 & \mu & 0 & 0 \\ 0 & 0 & 0 & 0 & \mu(1-\delta_T) & 0 \\ 0 & 0 & 0 & 0 & 0 & \mu(1-\delta_T) \end{pmatrix} . \qquad (25)$$

This stiffness matrix has transverse isotropy with a horizontal axis of symmetry oriented along the x_1 direction. The vertical velocity is in this case modified relative to the case of horizontal cracks, as δ_N is now multiplied by r^2 in the C_{33} term. This scales the *R*-factor R_{C4} such that $R_{C4} = r^2 R_{C1}$. For a typical V_P/V_S *of* 2, r^2 becomes $1/4$ – this point was mentioned also by Hatchell and Bourne (2005).

Table 3(b) shows the relative magnitudes of the *R*-factors as defined in equation (2) for the four classes of crack distribution given above. Although these classes relate to very different rock strain mechanisms, the *R*-values are very similar and differ at most by a factor of 4. However,

all do show that the mechanism of contact breakage is an efficient generator of large R-values. For contact creation upon compression, similar arguments would hold. The following is observed for an R defined by vertical velocity, V, and vertical strain, ε_{zz}, only: $R_{C1} > R_{C4} > R_{C2} > R_{C3}$. In practice, it may be possible to have more than one crack distribution (i.e., contact mechanism) present - for example, horizontal cracks plus random cracks. In this case, the result can be obtained by summing the individual contributions above in the compliance domain, weighted by the preponderance of each mechanism.

It can be concluded from the above and the seismic observations, that whilst the grain-grain contact mechanism per se has the potential to explain the anomalously large values that appear in our data, it may not be currently possible to differentiate between the particular 'crack' mechanisms causing extension and compression of the overburden or reservoir on the basis of vertical P-wave propagation alone. For this, more information is required – and this must come from offset and/or azimuthal dependency.

OFFSET-DEPENDENT TIME-SHIFTS

Measurements of time-shifts with offset/angle are of growing interest as high quality acquisitions are now available with sufficient offset coverage to measure these variations. There is therefore the possibility of using these as an additional source of information. Here we discuss the predictions of time-shift variations with offset or incidence angle for the semi-empirical model detailed above. We begin by discussing published observations in the open literature and also some data examples.

Observations of offset-dependent time-shifts

It is expected that time-lapse time-shifts should vary with offset/angle in seismic data, even if the time-lapse velocity changes themselves are isotropic. Landrø and Stammeijer (2004) predict this theoretically:

$$\Delta T = \int_0^T \left(\varepsilon_{zz} - (1 + \tan^2(\theta)) \frac{\Delta V}{V} \right) dt, \tag{26}$$

for a measurement at two-way time, T, and velocity, V, at angle θ. They demonstrate that measurement of these changes on the near and far-angle sub-stacks could be used to separate the combined influence of physical displacement, ε_{zz}, and velocity change, $\Delta V/V$. Observations of time-shifts with offset/angle have been published by only a small number of authors, these are shown in Table 4. For example, Herwanger, Palmer and Schiøtt (2007) measure time-shifts on the compacting chalk of the South Arne field, and conclude that they decrease with angle,

being 50% smaller at the further offsets. Hawkins (2008) on the other hand measures an increase with offset in the high pressure-high temperature (*HPHT*) Elgin field. Røste *et al.* (2007) measure time-shifts based on a permanent reservoir monitoring systems for the compacting chalk of the Valhall field using 2D seismic lines, observing offset-varying time shifts caused by a time-lapse velocity anomaly with small lateral extent. They are able to reproduce the observed offset-variation in the time shifts by building a synthetic velocity model representing a slipping fault. For cases where the velocity changes have larger lateral extent, the offset-variation in the time shifts will typically be less pronounced, and might therefore be more challenging to detect. Recently, Kudarova *et al.* (2016) presented examples of time-shifts obtained with angle sub-stacks of marine seismic data acquired in ocean bottom node (*OBN*) surveys in deep water (Gulf of Mexico, Mars) and narrow-azimuth streamer surveys in shallow water (North Sea, *HPHT* Shearwater). They did not observe a strong variation of time-shifts with offset as reported in previous publications. Additionally, despite OBN delivering a wide range of azimuthal coverage, they have observed no clear azimuthal dependence of the time-shift with offset behaviour to date*.

*[Footnote: Note that the reader might get the impression that offset-varying time-shifts are typically not present in 4D seismic data, however, there might be several reasons why these offset-variations are not available, e.g.: they have not been looked for in the data; they have not been published; the offset-variation is small and hard to detect; the processing of the pre-stack data is uncertain; noise makes the interpretation the offset-variation difficult.]

Predictions of time-shift dependence on incidence angle

For the Xu-White model and the isotropic orientation distribution of cracks, *ΔV/V* is an isotropic function of angle, and hence the analysis remains unchanged as in equation (24).

However for horizontal cracks, vertical cracks, or those with co-planar normals, $\Delta V/V$ needs to be calculated to take the anisotropic variations into account. For horizontally aligned cracks, the stiffness matrix has transverse isotropy with a vertical axis of symmetry. For this anisotropy, the phase velocity variation, $v(\theta)$, with incidence angle, θ, is specified by the Thomsen (1986) parameters, ε and δ:

$$v^2(\theta) = V^2(1 + 2\delta \sin^2 \theta \cos^2 \theta + 2\varepsilon \sin^4 \theta),\tag{27}$$

where

$$\varepsilon = \frac{C_{11} - C_{33}}{2C_{33}}\tag{28}$$

and

$$\delta = \frac{\left[(C_{13} + C_{44})^2 - (C_{33} - C_{44})^2\right]}{2C_{33}(C_{33} - C_{44})}.\tag{29}$$

The Thomsen parameters can be written in terms of the crack parameters for horizontal crack distributions

$$\varepsilon = 2g(1 - g)\delta_N\tag{30}$$

and

$$\delta = 2g(\delta_N - \delta_T).\tag{31}$$

We now find the phase velocity changes as a function of incidence angle

$$\frac{\Delta v}{v}(\theta) = \frac{\Delta V}{V}(0)\left[1 - 4g(1 - g)\sin^2 \theta - 4g^2(1 - B_T/B_N)\sin^2 \theta \cos^2 \theta\right]\tag{32}$$

or

$$\frac{\Delta v}{v}(\theta) = -R\varepsilon_{ZZ}\left[1 - 4g(1-g)\sin^2\theta - 4g^2(1 - B_T/B_N)\sin^2\theta\cos^2\theta\right] \tag{33}$$

This predicts that fractional phase velocity change decreases with incidence angle and scales with the *R*-factor defined previously. As the group velocity variation at the group angle may be approximated by the phase velocity variation at the group angle (determined by the offset ray) for the weak anisotropy approximation (Thomsen 1986), equation (32) is also valid for our travel-time computations where we replace $\frac{\Delta V}{V}$ in equation (26) by $\frac{\Delta v}{v}$. Figure 6 shows the resultant time-shift variation with angle (*TVA*), calculated for a range of V_P/V_S and B_T/B_N values. Importantly, the time-shift gradient for the anisotropic case is reduced or negative compared to the original isotropic prediction. Note, however, that the calculations here assume no lateral variations in the time-lapse changes, which are another clearly identifiable cause of time-shifts variations with offset (Røste *et al*. 2007) not considered in this current work. In practice, lateral variations must imprint upon the trends we predict from anisotropy through equation (33). Our result is consistent with previous work by Herwanger *et al.* (2007) who established through numerical modelling that a decrease with offset could be achieved using an anisotropic velocity variation calibrated by the third order coefficients on Prioul *et al*. (2004). Here, it is observed that the time-shift gradient is determined predominantly by the first term containing $g = (V_S/V_P)^2$, and to a lesser degree by the second term containing g and B_T/B_N. When g is small and $B_T/B_N < 1$, the net time-shift gradient in equation (26) can be negative. The factor B_T/B_N is recognized as relating to the nature and geometry (for example aspect ratio) of the internal rock damage (see for example, MacBeth and Schuett 2007). Many previous

laboratory and theoretical studies have concluded that $B_T/B_N < 1$ (e.g. Angus *et al*. 2009; Liu, Hudson and Pointer 2000; Verdon and Wuestefeld 2013). Hence, the second term may indeed reduce the overall time-shift gradient, especially for a shaley overburden for which V_P/V_S is large. The approximation $B_N = B_T$ is valid for thin, dry cracks (Sayers 2006), for this case $\varepsilon = \delta$ and the second term in equation (32) is zero and the gradient fixed only by g. This is a special case of a transversely isotropic (*TI*) system and the velocity dependence with angle of incidence is now elliptical and the wave surface is an ellipse.

For a random set of cracks, the post-production state is isotropic. In this case ε and δ are both zero and there is no additional velocity variation with incidence angle. For vertical cracks, the post-production state is *TI* with a horizontal symmetry axis. Thus, for a vertical plane of propagation aligned along the crack strike direction (i.e., in a plane of isotropy) the *TVA* gradient is positive. For a vertical plane of propagation perpendicular to the cracks, the variation is identical to equation (32), but with ϑ being replaced by $90 - \vartheta$. The gradient of $\Delta V/V$ now increases with incidence angle and thus enhances the existing isotropic variation (particularly if B_T is close to B_N). Thus, the magnitude of the *TVA* gradient along two mutually perpendicular sections can indicate whether the cracks are horizontal or vertical (or random). For a vertical plane of propagation between these two extremes, the *TVA* gradient varies with incidence angle and azimuth, and this can be calculated as a function of the angle with respect to the symmetry axis. Thus, $\sin\vartheta$ should be replaced by $\cos\vartheta\cos\phi$ and $\cos\vartheta$ by $\cos\vartheta\sin\phi$ in equation (32). There is now a predicted dependence on both incidence angle and azimuth. Although azimuthal effects are not currently observed in practice using *OBN* data, theoretical predictions suggest that scanning over both incidence angle and/or azimuth could potentially yield information regarding B_T/B_N if g is known.

It should be noted that the above result predicts a fairly moderate (5 to 20%) variation in time-shift with offset/angle, and a separation between the different classes of 'crack' distribution of the same amount. Such findings contrast with the much larger magnitude predictions from the 3rd order approach (Fuck *et al.* 2007) where the coefficients c_{111} and c_{112} have been calibrated using laboratory data (Prioul *et al*. 2004). We contend that our results appear closer to the data and provide a physical model for understanding the processes of rock mechanics in the subsurface.

DISCUSSION

This study began by outlining a number of key conclusions (I to VII) and current challenges ((a) to (e)) for the model that couples fractional velocity change to vertical strain. In response to these challenges, the relation proposed by Hatchell and Bourne (2005), and Røste et al. (2005), has been improved to better understand the underlying physical processes behind the R-factor magnitude. The magnitude of the R-factor across a range of lithologies is addressed by combining the compressibility of a dual-porosity volume with contact breakage/creation. It is thought that the hysteresis effect described in conclusion *IV* may be explained by inelastic effects related to contact breakage, especially in extension. The contact breakage also explains conclusion *VI* and the shear-wave birefringence in conclusion *VII*. Regarding conclusion *V*, it has also been shown that the R-factor model can be readily extended to provide an offset/angle dependence. This may explain the diversity in the observed variability of *TVA* gradient.

The general observations common to most field measurements in *I* and *II* are understood as $R_{ob}^{+} > R_{res}^{-}$. Our studies indicate that this inequality can be understood in three separate parts:

(1) *Lithology dependence* ‐ it has been shown that the magnitude of most of the observed R-factors (in the range 1 to 20 in Figure 3) can be matched to pore volume changes alone. The Xu-White model replicates the pore volume for a sand-shale system, and provides a straightforward route to calculate R for sandy shale or shaley sand. Application of the model for a realistic set of pore aspect ratios shows that rocks with a greater proportion of shale (or clay) will have larger R-factors than clean sands. Homogeneous chalk is predicted to have the smallest R-factors (1 to 2). R is also expected to increase with consolidation and cementation,

and in rocks with stiffer pore space. These findings mostly agree with both the field seismic data and laboratory data. In particular, as the overburden is likely to have a higher shale fraction than the reservoir, this partly explains the elevated R-factors due to the compliant shale-related pores. We believe that despite the current theoretical predictions being isotropic, this result will remain valid if the rocks were to be treated as initially anisotropic. A second category of 'anomalously high' (> 20) R-factors is also identified in our data: for example, in fractured chalk. These values are caused by grain-grain contact breakage or micro-fractures which enhance the sensitivity of the seismic velocity to changes in porosity. The magnitude of the R-factor is relatively insensitive to the orientation distribution of these crack sets, varying at most by a factor of 4. Thus, large R-factors are expected to be observed in fractured chalk formations in the overburden of the Shearwater field (Staples *et al.* 2007), and also within the chalk reservoir of Ekofisk (Janssen *et al*. 2007). Anomalously high values in the overburden can signal that the rocks have failed significantly and may be mechanically unstable and highly permeable. Negative R-factors are also predicted to be possible in the reservoir due to grain-grain contact crushing, and are again a sign of failure. This offers a possible explanation for the Malaysian example in Table 1 as collapse of the vugs in the carbonate under compression.

(2) *Stress/strain dependence* – the dependence of R on the stress/strain path is well documented from laboratory studies (Holt *et al*. 2016; Holt *et al*. 2008; Holt and Stenebråten 2013). Also, a significant stress path dependence of velocity stress sensitivity has been predicted by Sayers (2006) for a reservoir undergoing pore pressure increase and decrease. Using 3rd order elasticity theory to describe the triaxial strain dependence, Herwanger (2008) argues that direct use of the *HBR* model described by equation (2) neglects the horizontal strain components. The relative magnitude of R_{ob} versus R_{res} is therefore understood by the sensitivity of vertical velocity to differing triaxial strain. According to this theory, applying equation (2) to the zero

volumetric strain conditions of the overburden naturally yields a higher R than the uniaxial conditions of the reservoir. The R-factor predictions based on our pore volume and contact models also demonstrate a requirement to know the horizontal strain components in order to determine the overall volumetric strain. We therefore suggest that R in equation (2) could be modified to include this dependence by changing vertical strain to volumetric strain. That is

$$\frac{\Delta V}{V} = -R\varepsilon_{vol}.$$

(34)

However, it can be concluded that individual principal strain components cannot be separately estimated using the time-shift data.

(3) *Strain polarity asymmetry* – unfortunately there are insufficient data points for R_{res}^+ and R_{ob}^- to enable sensitivity to strain polarity to be strictly compared only in the reservoir or the overburden. It is therefore currently not possible to evaluate the relative magnitude of R^+ and R^- from 4D seismic data, although laboratory data do find that $R^+ > R^-$ (Holt *et al*. 2008). The pore volume model is sufficient to explain R_{res}^- values in the range 1 to 2, and R_{ob}^+ values of 5 to 20, but is not by itself polarity sensitive. It is possible that a few large or anomalously high R_{ob}^+ values observed are explained by a greater propensity for damage in extension rather than compression, and the inelastic processes of grain-grain contact breakage. Damage could therefore boost R^+ according to the theory described above and lead to polarity asymmetry. It is anticipated that this will be a function of the strain magnitude. A separate perspective is offered by Sayers (2006), who predicts asymmetry in velocity sensitivity with reservoir pore pressure (injection versus depletion in the reservoir) from stress dependent grain-grain contact compliances. Asymmetry of the velocity as a function of applied stress has also been measured

extensively in laboratory data (MacBeth 2004). For small strains, the exponential dependencies in these models can be approximated by the linear strain model, and it is this regime that is believed to be applicable to this current study. Rock damage can possibly be further assessed using time-shift versus offset/angle (*TVA*) analysis. This is because the *TVA* gradient could be used to estimate the parameter B_T/B_N, which could help determine if the damage that has occurred is from micro-fracturing. Azimuthal variations of the *TVA* gradient could provide an additional source of information regarding these effects. However, robust *TVA* or *TVA*-azimuth effects are relatively subtle and may not be detected with confidence by current acquisition and measurement techniques. Currently, time-shift variations with offset/angle remain useful for complex stress regimes and fault reactivation problems (Røste *et al*. 2007) where discrete velocity change anomalies are evident.

Speculation - finally, it is well known that whilst *P*-waves are clearly not as sensitive to cracks as shear waves (Crampin 1985), there is still clearly much potential in this technique due to the predominant use of the reflection seismic method in industry, and as almost all 4D surveys use *P*-wave recording. Should high quality shear-wave data become more readily available in industry, then clearly the assessment of failure in the overburden can be more precisely determined. In this case changes of shear-wave splitting are linked to the tangential compliance and another *R*-factor could be defined. Velocity changes with offset in this case may not be needed as a single measurement path may be sufficient.

CONCLUSIONS

It is shown that a simple dual pore-volume model can adequately explain the magnitude of the R-factors measured in observed 4D seismic data and select laboratory data. Anomalously high values occasionally observed in the overburden with field data or more extensively in the laboratory require a separate mechanism that simulates damage due to micro-fracturing or pore collapse. Based on these models, it can be deduced that the R-factor varies with lithology, being larger as shale content increases. $R_{ob} > R_{res}$ can be explained by a combination of lithology and stress path effects. The development in this study aligns with the original conceptual model of Hatchell and Bourne (2005), and Røste et al. (2005), but extends this work to offset/angle dependence. The subtle variation of the time-shift gradient with offset can be explained in terms of the orientation distribution of the internal rock damage. Whilst R remains the over-riding parameter controlling strain-sensitivity measured from 4D seismic data, B_T/B_N is a weaker parameter that may also prove of value. It is possible to estimate the parameter B_T/B_N from time-shift variation with offset, which could help assess the post-production state of the overburden. It is understood that observations of time-shift variation with angle must incorporate both these anisotropic effects and lateral variations in velocity change. The R-factor as originally defined for vertical P-wave propagation remains a useful generic parameter for monitoring the lithology-dependent strain state of the overburden, and to some degree the reservoir. It is not yet possible to precisely measure R-value variations across and throughout a field, however, the suggestion from our study is that this could be a useful tool for assessment of subsurface risk in the future.

ACKNOWLEDGEMENTS

REFERENCES

Angus D.A., Verdon J.P., Fisher Q.J. and Kendal J-M. 2009. Exploring trends in microcrack properties of sedimentary rocks: An audit of dry-core velocity-stress measurements. *Geophysics*, **74**, (5), E193 – E203.

Barkved O., Heavey P., Kjelstadli R., Kleppan T. and Kristiansen T.G., 2003. Valhall Field: Still on Plateau after 20 Years of Production, Offshore Europe, Aberdeen, SPE 83957

Bathija A.P., Batzle K.L. and Prasad M. 2009. An experimental study of the dilation factor. *Geophysics* **74**, (4), E181 – E191.

Brain J., Lassaigne T., Darnet M. and van Loevezijn P. 2017. Unlocking 4D seismic technology to maximize recovery from the pre-salt Rotliegend gas fields of the Southern North Sea. Proceedings of the 8th Petroleum Geology Conference.

Carcione J.M., Landrø M., Gangi A.F. and Cavallini F. 2007. Determining the dilation factor in 4D monitoring of compacting reservoirs by rock-physics models. *Geophysical Prospecting* **55**, 793 – 804.

Crampin S. 1985. Evaluation of anisotropy by shear-wave splitting. *Geophysics* **50**, 142 – 152.

Davis E., Wright C., Demetrius S., Choi J. and Craley G. 2000. Precise tiltmeter subsidence monitoring enhances reservoir management. *SPE/AAPG Western regional Meeting*, Long Beach, California, SPE 62577-MS.

De Gennaro S., Grandi A., Escobar I., Onaisi A., Ben-Brahim L., Joffroy G., Tindle C. and Neillo V. 2008. Integrating 4D seismic, Geomechanics and Reservoir simulations in the Elgin and Franklin fields. 70th EAGE Annual Meeting, Rome, Italy, Extended Abstracts, E019.

Doornhof D., Kristiansen T.G., Nagel N.B., Pattilo P.D. and Sayers C., 2006. Compaction and subsidence. *Schlumberger Oilfield Review* **18**, (3), 50 - 68.

Dunn S., Hatchell P., van den Beukel A., de Vries R. and Frafjord T. 2016. A long-term seafloor deformation monitoring campaign at Ormen Lange gas field. *First Break* **34**, (10), 55 – 64.

Ebaid H., Nasser M., Hatchell P.J. and Stanley D. 2009. Time-lapse seismic makes a significant business impact at Holstein. 79th SEG Annual Meeting, Houston, Texas, Expanded abstracts, 3810 – 3814.

Fehmers G.C., Hunt K., Brain J.P., Bergler S., Kaestner U., Schutjens P.M. and Burrell R.V. 2007. Curlew D – pushing the boundaries of 4D depletion signal in a gas condensate field, UK central North Sea. 79th EAGE Annual Meeting, London, UK, Extended Abstracts, P074.

Fuck R.F., Bakulin A. and Tsvankin I. 2007. Time-lapse travel-time shifts above compacting reservoirs: 3D solutions for prestack data. 77th SEG Annual Meeting, San Antonio, Texas, Expanded Abstracts, 2929 – 2933.

Fuck R.F., Bakulin A. and Tsvankin I. 2009. Theory of traveltime shifts around compacting reservoirs: 3D solutions for heterogeneous anisotropic media. *Geophysics* **74**, (1), D25–D36.

Floricich M. 2006. An engineering-consistent approach for pressure and saturation estimation from time-lapse seismic data. PhD thesis, Heriot-Watt University, Edinburgh, UK.

Geertsma J. 1973. Land subsidence above compacting oil and gas reservoirs. *Journal of Petroleum Technology* **25**, (6), 734–744.

Hall S.A., MacBeth C., Barkved O.I. and Wild P. 2002. Time-lapse seismic monitoring of compaction and subsidence at Valhall through cross-matching and interpreted warping of 3D streamer and OBC data. 72nd SEG Annual Meeting, Salt Lake City, Utah, Expanded Abstracts, 1696 – 1699.

Hatchell P.J., van den Beukel A., Molenaar M.M., Maron K.P., Kenter C.J., Stammeijer J.G.F., van der Velde J.J. and Sayers C.M. 2003. Whole earth 4D: reservoir monitoring geomechanics. 73rd SEG Annual Meeting, Dallas, Texas, Expanded Abstracts, 1330–1333.

Hatchell P. and Bourne S. 2005. Rocks under strain: Strain-induced time-lapse time shifts are observed for depleting reservoirs. *The Leading Edge* **24**, (12), 1222–1225.

Hatchell P.J., Kawar R.S. and Savitski A.A. 2005. Integrating 4D Seismic, Geomechanics and Reservoir Simulation in the Valhall Oil Field. 67th EAGE Annual Meeting, Madrid, Spain, Extended Abstracts, C012.

Hatchell P.J., Jorgensen O., Gommesen L. and Stammeijer J. 2007. Monitoring reservoir compaction from subsidence and time-lapse time shifts in the Dan field. 77th SEG Annual Meeting, San Antonio, Texas, Expanded Abstracts, 26, 2867 – 2871.

Hatchell P., Willis P. and Didraga C. 2009. Production induced effects on near-surface wave velocities at Valhall. 71st EAGE Annual Meeting, Amsterdam, The Netherlands, Extended Abstracts, T016.

Hawkins K., Howe S., Hollingworth S., Conroy G., Ben-Brahim L., Tindle C., Taylor N., Joofroy G. and Onaisi A. 2007. Production- induced stresses from time-lapse time shifts: A geomechanics case study from Franklin and Elgin fields. *The Leading Edge* **26**, (5), 655–662.

Hawkins K. 2008. Defining the extent of the compacting Elgin reservoir by measuring stress induced Anisotropy. *First Break* **26**, (10), 81 – 88.

Herwanger J., Palmer E. and Schiøtt C.R. 2007. Anisotropic velocity changes in seismic time-lapse data. 77th SEG Annual Meeting, San Antonio, Texas, Expanded Abstracts, 2883–2887.

Herwanger J.V. 2008. R we there yet? 70th EAGE Annual Meeting, Rome, Italy, Extended Abstracts, I029.

Hodgson N. 2009. Inversion for reservoir pressure change using overburden strain measurements determined from 4D seismic. PhD thesis, Heriot-Watt University, Edinburgh, UK.

Hodgson N., MacBeth C., Duranti L., Rickett J. and Nihei K. 2007. Inverting for reservoir pressure change using time-lapse time strain Application to Genesis Field Gulf of Mexico. *The Leading Edge* **26**, (5), 649 – 652.

Holt R.M., Nes O-M. and Fjaer E. 2005. In-situ dependence of wave velocities in reservoir and overburden rocks. *The Leading Edge* **24**, (12*), 1268 – 1274.

Holt R.M., Fjaer E., Nes O-M. and Stenebråten J.F. 2008. Strain Sensitivity of Wave Velocities in Sediments and Sedimentary Rocks. *42nd US Rock Mechanics Symposium and 2nd U.S.- Canada Rock Mechanics Symposium, San Francisco, June 29- July 2, ARMA-08-291.*

Holt R. M. and Stenebråten J. F. 2013. Controlled laboratory experiments to assess the geomechanical influence of subsurface injection and depletion processes on 4D seismic responses. *Geophysical Prospecting* **61**, 476 – 488.

Holt R., Bauer A., Bakk A. and Szewczyk D. 2016. Stress path dependence of ultrasonic and seismic velocities in shale. 86th SEG Annual Meeting, Dallas, Texas, Expanded Abstracts, 3159 – 3163.

Janssen A.L., Smith B.A. and Byerley G.W. 2007. Measuring seismic velocity sensitivity to production-induced strain at the Ekofisk field. Offshore Technology Conference, Houston, Texas, OTC-18700-MS.

Jones M.E., Leddra M.J., Goldsmith A.S. and Edwards D. 1992. The Geomechanical Characteristics of Reservoirs and Reservoir Rocks. *UK Health and Safety Executive Offshore Technology Report OTH333*.

Kazinnik R., Roy B., Tura A., Vedvik L. and Knoth O. 2014. Near surface velocities at Ekofisk from Scholte and refracted wave analysis. 84th SEG Annual Meeting, Denver, Colorado, Expanded abstracts, 2036 – 2039.

Keys R.G. and Xu S. 2002. An approximation for the Xu-White velocity model. *Geophysics* **67**, 1406 – 1414.

Kudarova A., Hatchell P., Brain J. and MacBeth C. 2016. Offset-dependence of production-related 4D time-shifts: real data examples and modeling. 86th SEG Annual Conference, Dallas, Texas, Expanded Abstracts, 5395 – 5399.

Landau L.D. and Lifshitz E.M. 1986. *Theory of Elasticity*, Pergamon Press.

Landrø M. and Stammeijer J. 2004. Quantitative estimation of compaction and velocity changes using 4D impedance and travel time changes. *Geophysics* **69**, 949 – 957.

Liu E., Hudson J.A. and Pointer T. 2000. Equivalent medium representation of fractured rock. *Journal of Geophysical Research* **105**, 2981 – 3000.

MacBeth C. 2004. A classification for the pressure-sensitivity properties of a sandstone rock frame. *Geophysics* **69**, 497 – 510.

MacBeth C. and Schuett H. 2007. The stress dependent elastic properties of thermally induced microfractures in aeolian Rotliegend sandstone. *Geophysical Prospecting* **55**, 323 – 332.

MacBeth C., Mangriotis M-D. and Amini H. 2018. A review of 4D seismic time-shifts, Part 1: values and interpretation. *Geophysical Prospecting*, In Press.

MacBeth C., Stammeijer J. and Omerod M. 2006. Seismic monitoring of pressure depletion evaluated for a United Kingdom continental-shelf gas reservoir. *Geophysical Prospecting* **54**, 29 – 47.

Mavko G., Mukerji T and Dvorkin J. 2009. *The Rock physics handbook, Second Edition*, Cambridge University Press.

Murnaghan F. 1937. Finite Deformations of an Elastic Solid. *American Journal of Mathematics* **59**, 235 – 260.

Nur A. and Simmons G. 1969. Stress-induced velocity anisotropy in rock: an experimental study. *Journal of Geophysical Research* **74**, 6667 - 6674.

Olofsson B., Probert T., Kommedal J.H. and Barkved O. 2003. Azimuthal anisotropy from the Valhall 4D 3D survey. *The Leading Edge* **22**, (12), 1228 – 1235.

Pettijohn F.J., Potter P.E. and Siever R. 1987. Sand and sandstone, Springer, New York.

Prioul R., Bakulin A. and Bakulin V. 2004. Nonlinear rock physics model for estimation of 3D subsurface stress in anisotropic formations: Theory and laboratory verification. *Geophysics* **69**, 415 – 425.

Raikes S., Mathieson A., Roberts D. and Ringrose P. 2008. Integration of 3D seismic with satellite imagery at In Salah CO2 sequestration project, Algeria. 78th SEG Annual Meeting, Las Vegas, Nevada, Expanded Abstracts, 5368 – 5372.

Rickett J., Duranti L., Hudson T., Regel B. and Hodgson N. 2007. 4D time strain and the seismic signature of geomechanical compaction at Genesis. *The Leading Edge* **26** (5), 644 – 647.

Rodriguez-Herrera A., Koutsabeloulis N., Onaisi A., Fiore J. and Selva F. 2015. Stress-induced signatures in 4D seismic data: evidence of overburden stress arching. 85th SEG Annual Meeting, New Orleans, Louisiana, Expanded Abstracts, 5368 – 5372.

Røste T., Stovas A. and Landrø M. 2005. Estimation of layer thickness and velocity changes using 4D prestack seismic data. 67th EAGE Annual Meeting, Madrid, Spain, Extended Abstracts, C010.

Røste T., Landrø M. and Hatchell P. 2007. Monitoring overburden layer changes and fault movements from time-lapse seismic data on the Valhall Field. *Geophysical Journal International* **170,** 1100 – 1118.

Røste T., Dybvik O.P. and Søreide O.K. 2015. Overburden 4D time-shifts induced by reservoir compaction at Snorre field. *The Leading Edge* **34**, (11), 1366 – 1374.

Røste T. and Ke G. 2017. Overburden 4D time shifts – Indicating undrained areas and fault transmissibility in the reservoir. *The Leading Edge* **36**, 423-430.

Sarkar D., Bakulin A. and Kranz R.L. 2003. Anisotropic inversion of seismic data for stressed media: Theory and a physical modelling study on Berea sandstone. *Geophysics* **68**, 690 – 704.

Sayers C. M. and Kachanov M. 1995. Microcrack-induced elastic wave anisotropy of brittle rocks. *Journal of Geophysical Research* **100**, 4149 – 4156.

Sayers C.M**.** 2006. Sensitivity of time-lapse seismic to reservoir stress path. *Geophysical Prospecting* **54**, (3), 369-380; Erratum: **54**, (5), 662-662. [Erratum: Geophysical prospecting **54**, 662 – 662]

Schutjens P.M.T.M., Hanssen T.H., Hettema M.H.H., Merour J., de Bree P., Coremans J.W.A. and Helliesen G. 2004. Compaction-induced porosity/permeability reduction in sandstone reservoirs: Data and model for elasticity-dominated deformation. *SPE Reservoir Evaluation and Engineering* **7**, SPE 88441, 202 – 215.

Simm R. and Bacon M. 2014. *Seismic amplitude: An interpreter's handbook*. Cambridge University Press, Cambridge.

Staples R., Ita J., Burrell R. and Nash R. 2007. Monitoring pressure depletion and improving geomechanical models of the Shearwater field using 4D seismic. *The Leading Edge* **26**, (5), 636 – 642.

Thomsen L. 1986. Weak elastic anisotropy. *Geophysics* **51**, 1954 – 1966.

Van Bergen P.F., de Gennarro S., Fairhurst F., Hurry R., Concho M., Watson J., Sturgess L. and Bevaart M. 2013. Shearwater-securing the chalk – effects of depletion of a HPHT reservoir on chalk overburden. SPE offshore Oil and Gas conference and exhibition, Aberdeen, *SPE 166574*.

Van Gestel P-G., Kommedal, J., Barkved O., Mundal I., Bakke R. and Best K. 2008. Continuous seismic surveillance of Valhall Field. *The Leading Edge* **27**, (12), 1616–1621.

Vega S.D.R. 2003. Intrinsic and stress-induced velocity anisotropy in unconsolidated sands. PhD thesis, University of Stanford, Stanford, USA.

Verdon J.P. and Wuestefeld A. 2013. Measurement of the normal/tangential fracture compliance ratio (ZN/ZT) during hydraulic fracture stimulation using S-wave splitting data. *Geophysical Prospecting* **61**, 461 – 475.

Wang Z. 2002. Seismic anisotropy in sedimentary rocks, part 2: Laboratory data. *Geophysics* **67**, 1423 – 1440.

Wong M. and MacBeth C. 2016. R-factor recovery via Geertsma's pressure inversion assisted by engineering concepts. 78th EAGE Annual Meeting, Vienna, Austria, Extended Abstracts, WS14.

Xu S. and White R. E. 1995. A new velocity model for clay-sand mixtures. *Geophysical Prospecting* **43**, 91–118.

Zimmerman R.W. 1991. *Compressibility of sandstones*. Developments in Petroleum Science 9, Elsevier, Amsterdam.

Field	R factor values		Subsidence measured?	In situ measurements?	Reservoir Lithology	Reference	Comments
	R^+ overburden	R^- reservoir					
Valhall	4 to 9	< 2	Yes	Yes	Chalk	Hatchell et al. 2005	
Ekofisk	4 to 10	2	Yes	Yes	Overburden & chalk reservoir	Janssen et al. (2007)	Streamer data
Ekofisk	25	16	No	No	Chalk	Wong and MacBeth (2016)	LoFS
Dan	4 to 6		Yes	No	Chalk	Hatchell et al. (2007)	
Holstein	5 to 10	< 1	No	No	Clastics	Ebaid et al. (2009)	Compressibilities
Malaysia		-1.5 to 0.5	No	No	Carbonate	Private communication	
Shearwater	4 to 6	1 to 3	Yes	No	HPHT Clastics	Van Bergen et al. (2013)	At platform
Mars	4 to 8	< 2	Yes	Yes	Clastics	Hatchell and Bourne (2005)	
Shearwater	20 to 35		No	No	HPHT Clastics	Staples et al. (2007)	OB Chalk group
Elgin-Franklin	7		No	No	HPHT Clastics	Hawkins et al. (2007)	
Elgin-Franklin	20 to 100		No	No	HPHT Clastics	De Gennaro et al. (2008)	OB Chalk group
Snorre	20		No	No	Unconsolidated sands	Røste et al. (2015)	
Genesis	5		No	No	Unconsolidated sands	Hodgson et al. (2007)	
Statfjord	15		Yes	No	Clastics	Røste and Ke (2017)	3D modelling. Also Snorre and Heidrun

Table 1 *R*-factors calculated for the overburden and reservoir for a variety of field settings, together with the data used to constrain these observations. Only R_{ob}^+ and R_{res}^- are shown, as values for R_{ob}^- and R_{res}^+ are not typically reported and data points are still actively sought for these important parameters.

R values		Lithology	Uniaxial loading	Hydrostatic loading	Reference	Comments
R^+	R^-					
	0 to 150	Ottowa sand Valgrinda sand			Holt et al. (2008)	Unconsolidated, zero at failure
	0 to 50	Cemented sandstone			Holt et al. (2008)	zero upon sample failure
10 to 27, 5 to 14	19 to 28, 1 to 5	Synthetic sandstone			Holt et al. (2008)	Extensive loading/unloading tests
	6 to 91	Sandstone			Bathija et al. (2009)	
55, 75	15	Synthetic sandstone			Holt and Stenebråten (2013)	Uniaxial loading and unloading
147, 283, 304		Fine to coarse grained sand			Vega (2003)*	Calculated by Bathija et al. (2009)
729		Dry Berea sandstone			Sarkar et al. (2003)*	Calculated by Bathija et al. (2009)
40 to 45		Brine saturated shale			Wang (2002)*	Calculated by Bathija et al. (2009)
10 to 30		Chalk			Janssen et al. (2007)	
34 to 50, 13	34 to 50, 6	Shale			Holt et al. (2008)	
5 to 6	1 to 3	Artificial claystone			Holt et al. (2008)	Loading/unloading tests
	6 to 11	Shale			Bathija et al. (2009)	
	2 to 3	Synthetic shale			Holt and Stenebråten (2013)	Loading under constant mean stress

Table 2 *R*-factors calculated in the laboratory for a variety of rocks and stress/strain conditions. * - calculated by Bathija *et al.* (2009).

(a)

α_{sa}	α_{cl}	V_{cl}	Φ (%)	R^+ and R^-	Lithology
0.15	0.02	0	25	1.4	Shaley sand (R_A)
0.27	0.04	0	25	0.8	Shaley sand – stiff (R_A)
0.15	0.02	0.6	5	6.0	Sandy shale (R_A)
0.27	0.04	0.6	5	3.0	Sandy shale – stiff (R_A)
0.27	-	-	25	0.8	Stiff sandstone pores (R_A)
0.65	-	-	25	0.5	Porous chalk (R_A)
0.65	0.01	0.1	25	2.7	Fractured porous chalk (R_A)
-	0.01	-	5	19.9	Only fractures (R_A)
0.15	0.02	0	25	1.0	Shaley sand (R_B)
0.27	0.04	0	25	1.2	Shaley sand – stiff (R_B)
0.15	0.02	0.6	5	95	Sandy shale (R_B)
0.27	0.04	0.6	5	28	Sandy shale – stiff (R_B)

(b)

α	Φ (%)	R^+ or R^-	Crack distribution
0.001	25	750	Horizontal cracks (R_{C1})
0.001	25	975	Random cracks (R_{C2})
0.001	25	435	Random crack normals (R_{C3})
0.001	25	187	Vertical cracks (R_{C4})
0.01	25	75	Horizontal cracks (R_{C1})
0.01	25	96	Random cracks (R_{C2})
0.01	25	44	Random crack normals (R_{C3})
0.01	25	19	Vertical cracks (R_{C4})

Table 3 (a) Uniaxial strain path R-values for a selection of aspect ratios and lithologies calculated using the Xu and White (1995) model for the dry rock frame only – the R_A and R_B values are described in the main text. Top four rows are for size changes only – thus, R_A values. Bottom four rows refer to the model in which the aspect ratios are varied to simulate porosity change – R_B values. The middle four rows are R_A values for specific scenarios. (b) R-values for the four contact breakage scenarios described in the main text (defined as R_{C1}, R_{C2}, R_{C3} and R_{C4}), for two selected aspect ratios and a background rock with V_P/V_S=2.
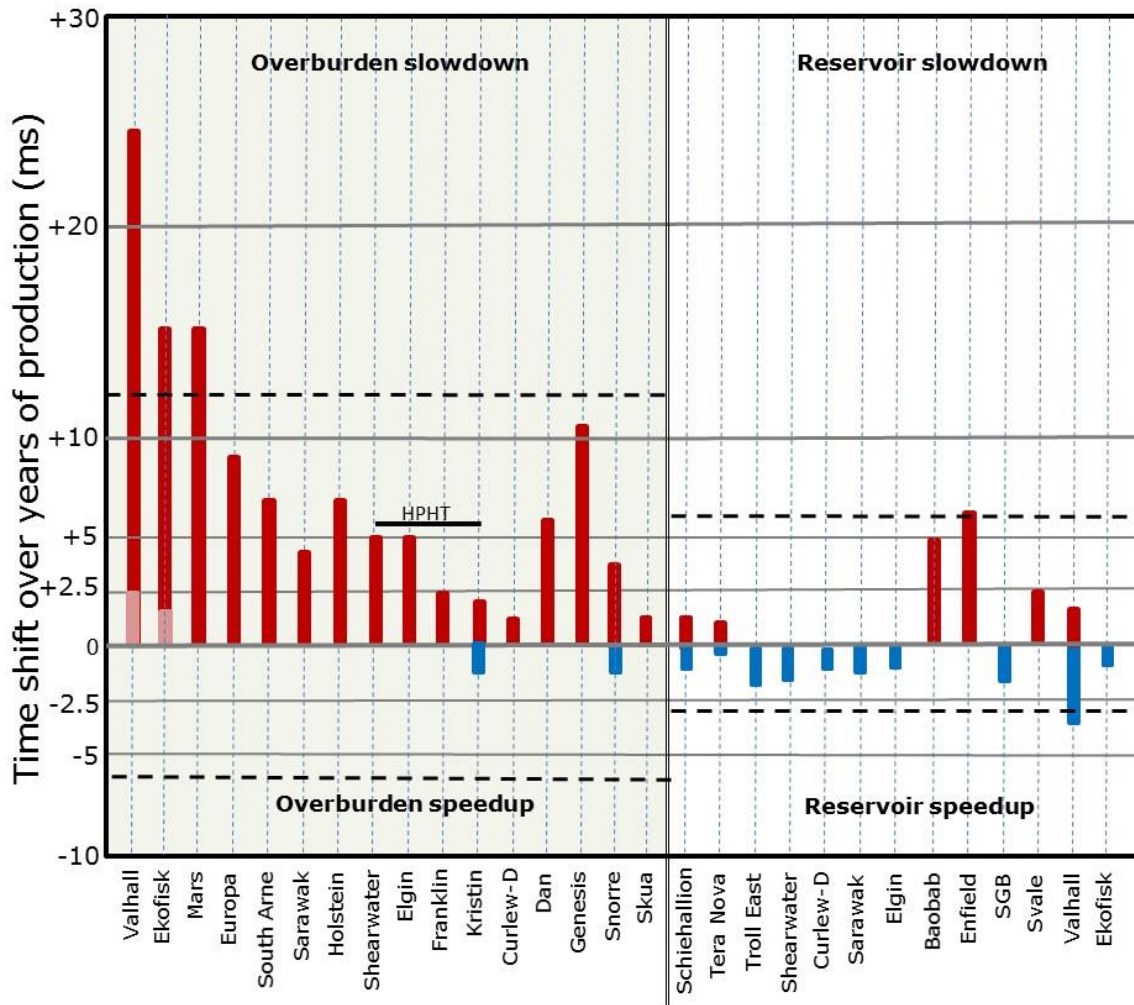
G	Field	Publication
0.50	South Arne	Herwanger et al. (2007)
Increase	Elgin	Hawkins (2008)
Various	Valhall	Røste et al. (2007)
Close to zero	Shearwater	Kudarova et al. (2016)
Small increase	Mars	Kudarova et al. (2016)

Table 4 Approximate estimates of the time-shift with offset/angle gradient $G = (\Delta T_{far} - \Delta T_{near})/\Delta T_{near}$ published in open literature and also observed by the authors. Most results are purely qualitative in nature to date and uncertainty still remains.

FIGURES
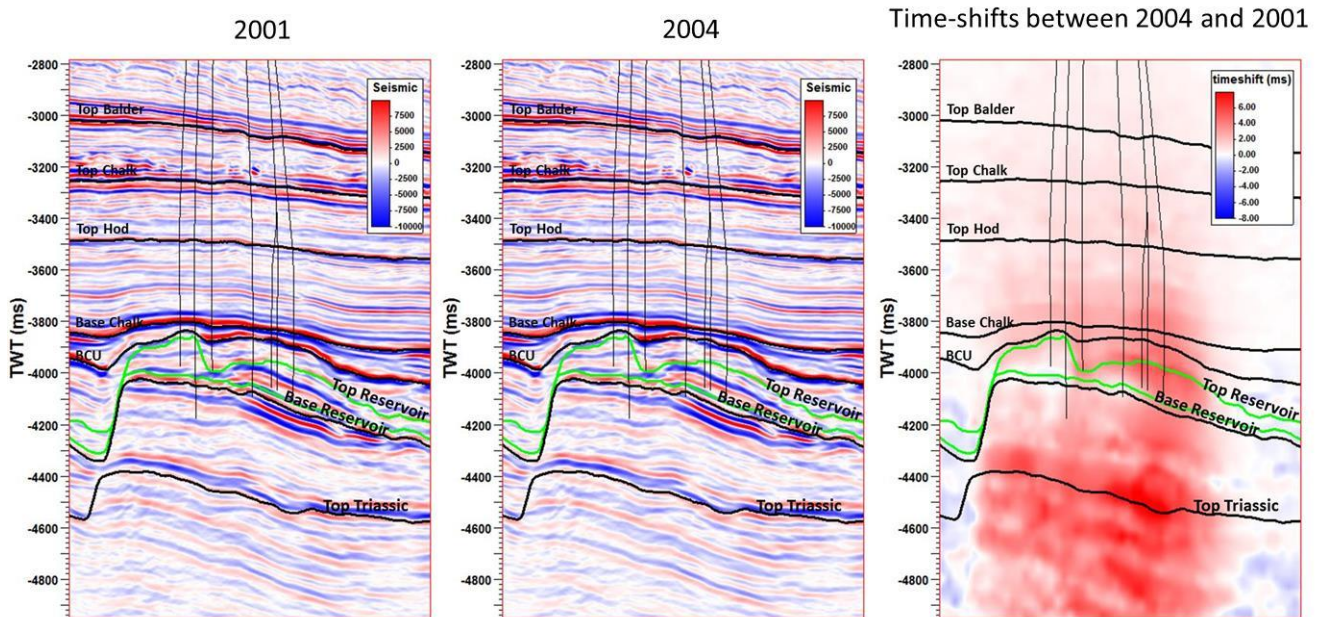
Figure 1 Example of vertical sections for baseline and monitor seismic data, together with the time-shifts measured between the two datasets. The positive time-shifts indicate that overburden rock is extending as a result of compaction in the reservoir (visible as a slight reduction in the time-shift variation with two-way time). The velocity strain sensitivity in this case is governed by the factor R_{ob}^{+} in the overburden and R_{res}^{-} in the reservoir. Key horizons are drawn on the seismic sections for reference. The sections are migrated using the baseline velocity model.

Figure 2 Observed maximum time-shifts for a range of field datasets reported in the open literature (adapted from MacBeth *et al.* 2018). Values are reported as attributed to overburden or reservoir as recorded by the authors of the publications. For reference only, dashed lines are drawn to represent a 2000ms overburden with a uniform mean vertical strain of 10^{-3}. Also shown are dashed lines for a 100ms reservoir with a vertical strain of 10^{-2}. For these calculations the *R*-factor for extension is $R^+ = 5$ and for compaction $R^- = 2$. The reservoir measurements may also be contaminated by fluid changes, and are thus not wholly representative of the geomechanical effects.
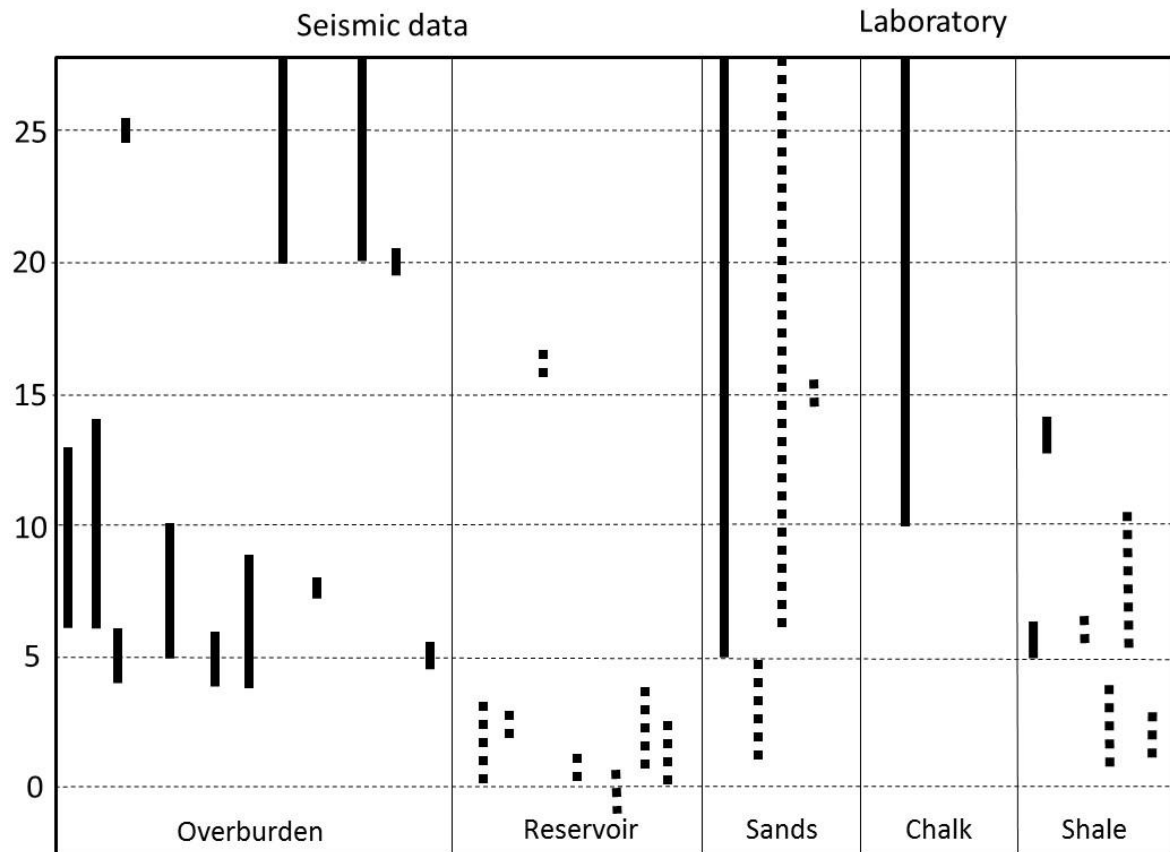
Figure 3 The range of *R*-factors estimated from observed seismic data and also from the laboratory extracted from published literature and datasets to date (corresponding to Tables 1 and 2). Those determined for extension R^+ are designated by solid lines, whilst the dashed lines are for those values determined for compression R^-. Values higher than 25 are not shown for clarity (see Table 2 for details).
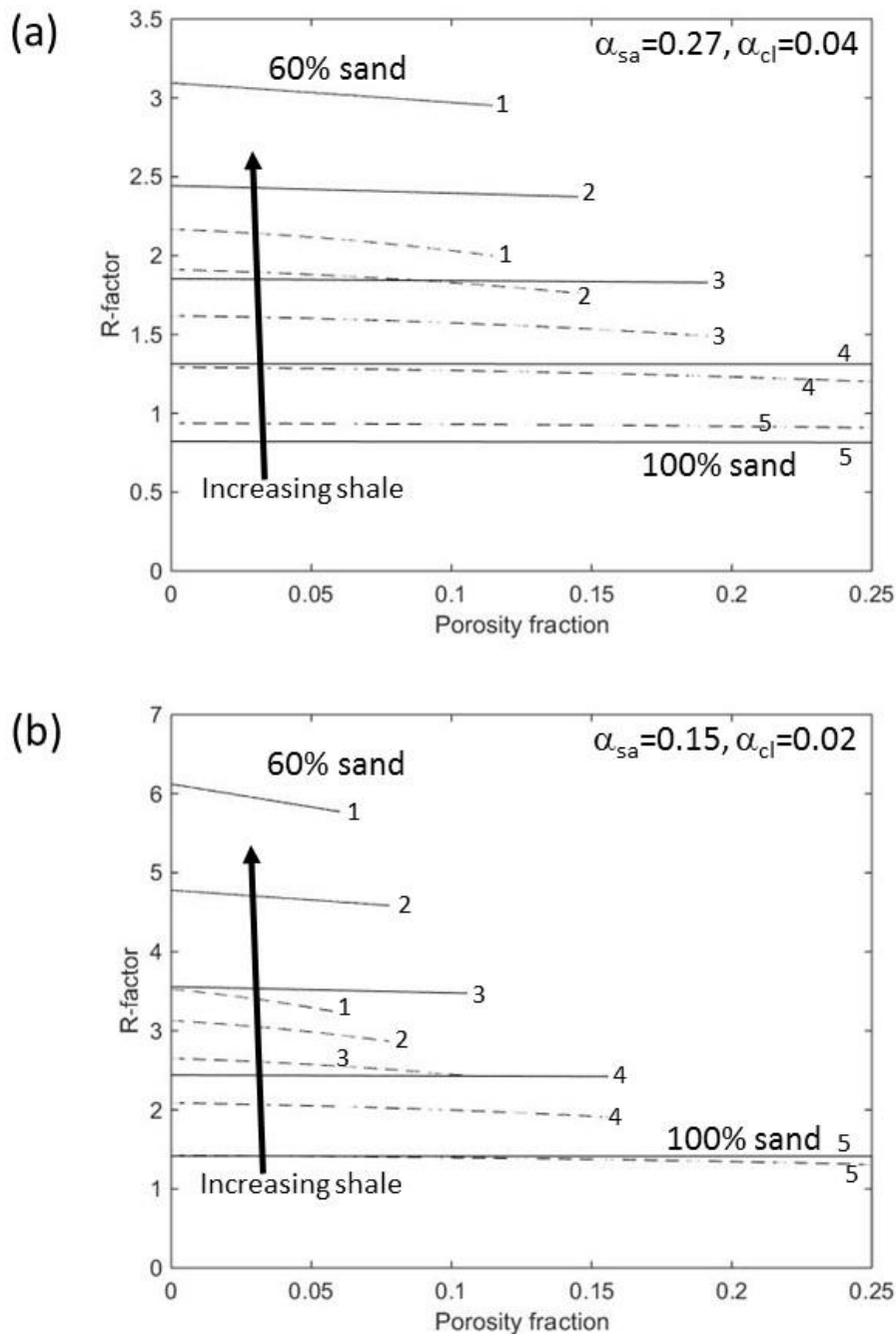
Figure 4 *R*-factors for pore size change only (i.e. R_A described in the main text) calculated using the Xu-White (1995) model for two aspect ratio combinations typically used to model sand-shale systems, as a function of the fractional porosity. (a) Sand and shale aspect ratios of 0.27 and 0.04 respectively; (b) sand and shale aspect ratios of 0.15 and 0.02. Solid lines are for the dry rock, and dashed lines are for brine-filled rock. Lines 1 to 5 are drawn for 10% increments of shale fraction, from 40% shale (sandy shale) to 100% sand. For all cases the lines terminate at the critical porosity as defined by Keys and Xu (2002) – see main text.
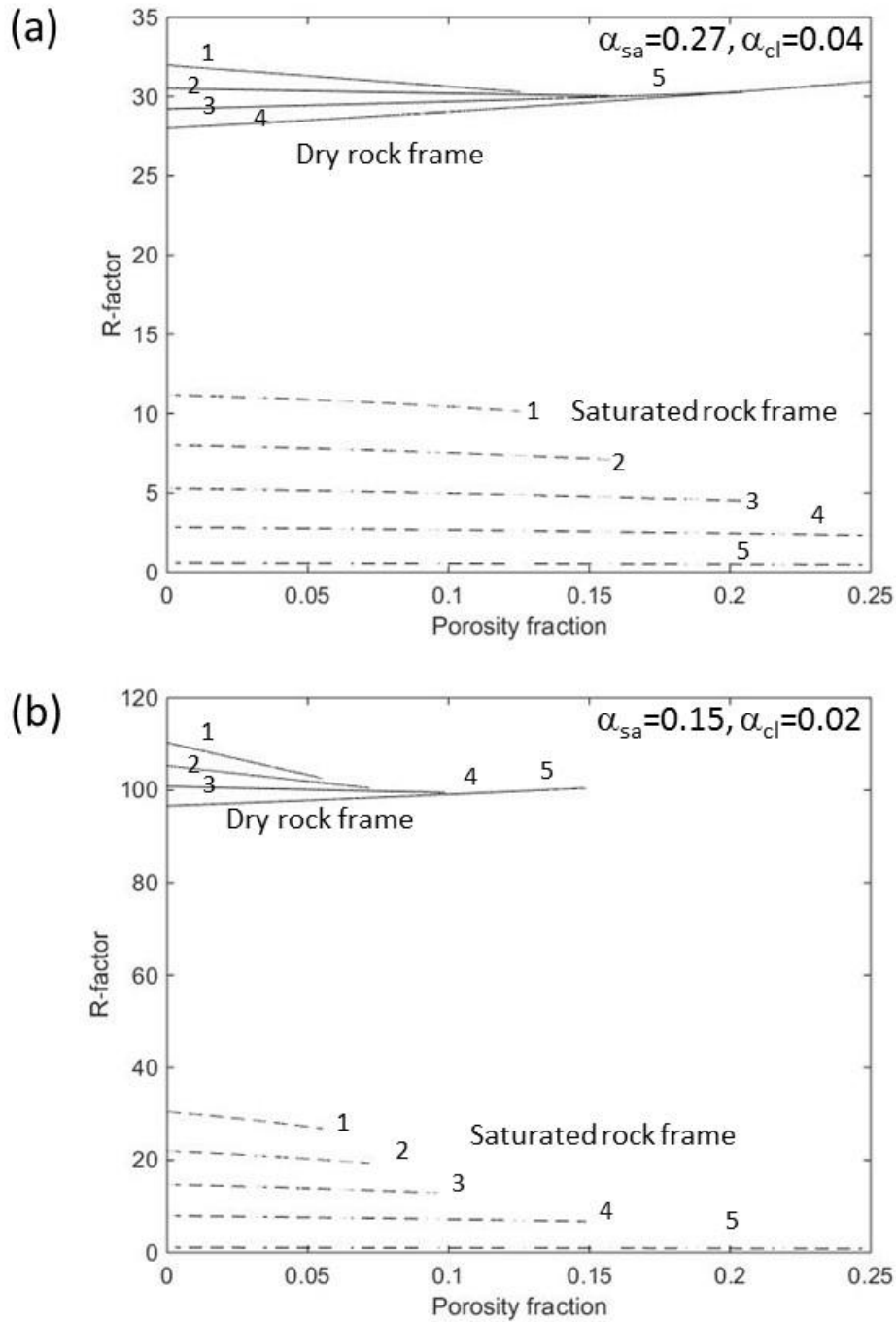
Figure 5 *R*-factors calculated using the Xu-White (1995) model based on a change of aspect ratio with strain (i.e. the R_B values described in the main text). As in Figure 4, two commonly quoted aspect ratio combinations are employed: (a) Sand and shale aspect ratios of 0.27 and 0.04 respectively; (b) sand and shale aspect ratios of 0.15 and 0.02. Solid lines are for the dry rock, and dashed lines are for brine-filled rock. Lines 1 to 5 are drawn for 10% increments of shale fraction, from 100% sand (5) to 60% sand (1, sandy shale). For all cases the lines terminate at the critical porosity as defined by Keys and Xu (2002) – see main text.
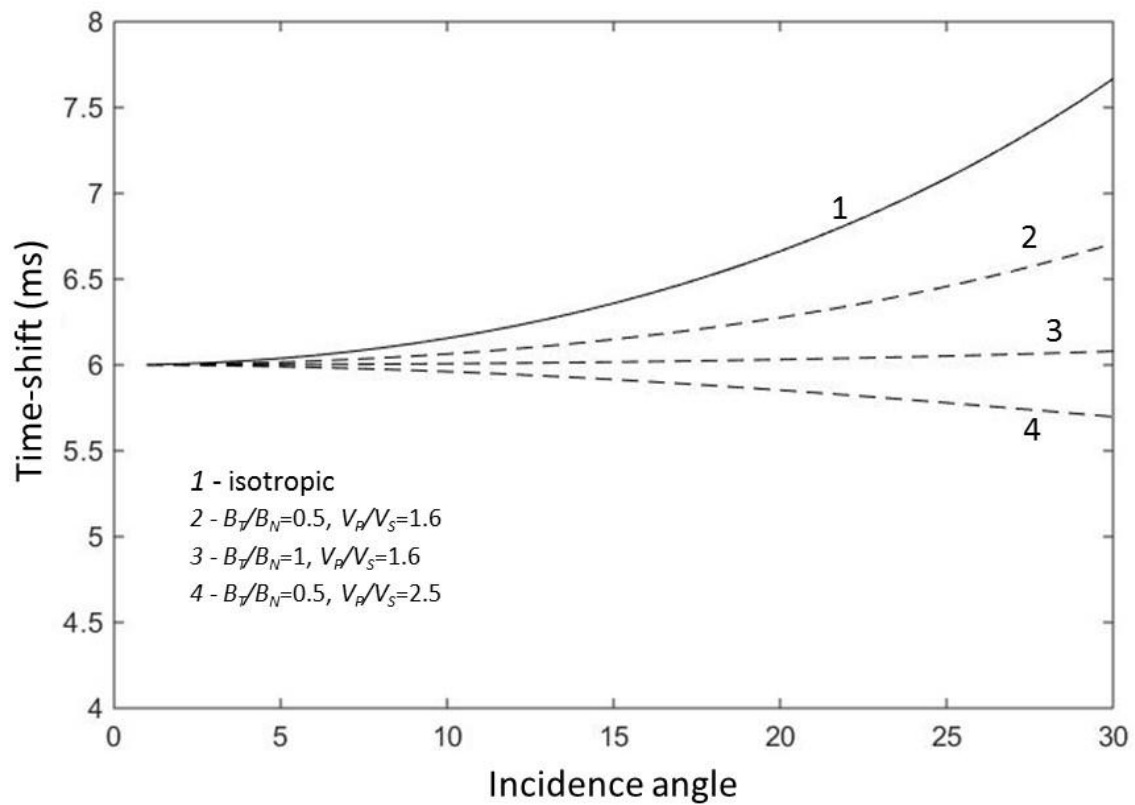
Figure 6 Time-shifts as a function of offset for a VTI overburden, and then three select combinations of V_P/V_S and B_T/B_N for the horizontal crack model. The isotropic R-factor for this calculation is 5, and a uniform strain of 10^{-3} is assumed.